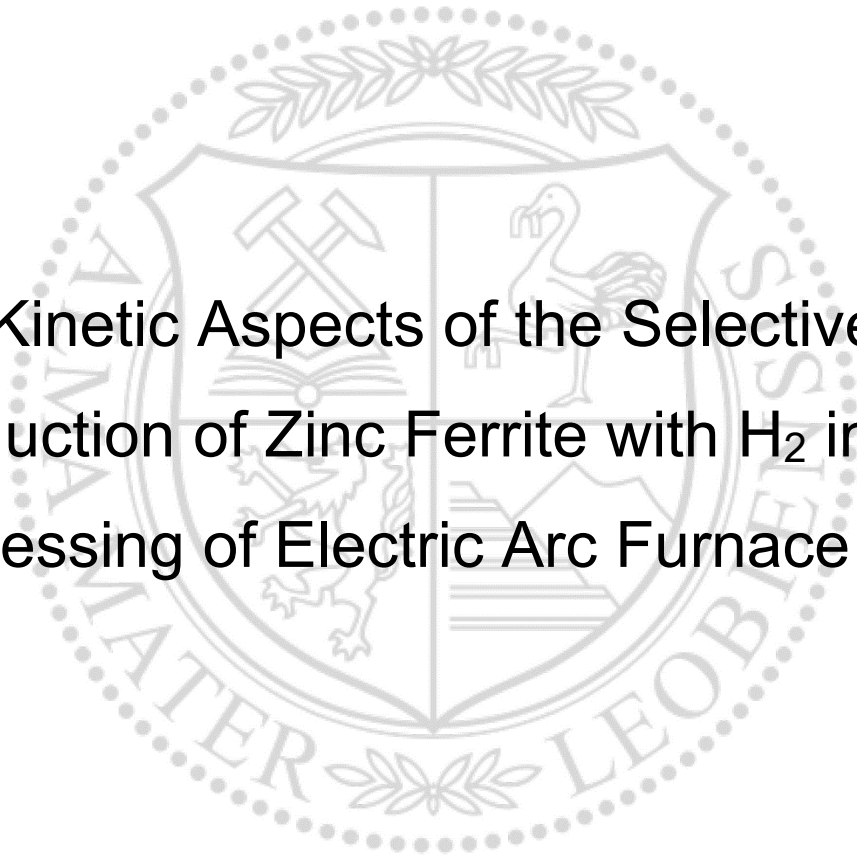Chair of Nonferrous Metallurgy

Master´s Thesis

Kinetic Aspects of the Selective Reduction of Zinc Ferrite with H_2 in the Processing of Electric Arc Furnace Dust

Felix Hoffelner, BSc

September 2022

Danksagung

Ich möchte mich herzlich bei allen Mitarbeitern des Lehrstuhls für Nichteisenmetallurgie bedanken, welche in diese Arbeit, und insbesondere die Versuche dazu, involviert waren. Ausdrücklich möchte ich hier Ulrich Brandner und Manuel Leuchtenmüller nennen, die mich bei fachlichen Fragen zu praktischen und theoretischen Problemen stets unterstützten. Außerdem gilt mein Dank Familie und Freunden, welche mir in dieser Zeit im Privaten zur Seite standen. Ohne die genannten Personen wäre diese Arbeit nicht möglich gewesen.

Abstract

EAF dust is currently recycled via processes that rely on carbothermal reduction. The implementation of an H_2-based reduction process could help reduce greenhouse gas emissions in a way that would allow recyclers to contribute their part to the European Green Deal. Although some studies already proved technical feasibility, a definitive process has yet to be established. A key role plays the reaction kinetics between the solid EAF dust constituents and the gaseous H_2. This work investigated the relevant reactions in thermogravimetric experiments using high-purity $ZnFe_2O_4$ and Fe_2O_3 powders. The results from the pure substances were then compared to experiments using pure EAF dust. The objective was to study the kinetics of the individual sequential reduction steps. Kinetic models for the individual reduction steps of $ZnFe_2O_4$ and Fe_2O_3 could be found, but some ambiguities remained for the Fe_2O_3 results. The results indicate a different behaviour between iron oxide reduction from $ZnFe_2O_4$ and Fe_2O_3. The main difference lies in the first two reduction steps up to FeO, which for $ZnFe_2O_4$ is rate limited by nucleation and diffusion. The limiting mechanisms for Fe_2O_3 appear to be nucleation and growth. The final reduction step to metallic Fe proceeds in a similar overall manner for both materials and follows a geometric contraction model. The behaviour of EAF dust shows similarities with that of $ZnFe_2O_4$. Although, a comprehensive kinetic study with a special focus on EAF dust has yet to be conducted. Further experiments should investigate the same reactions in an extended parameter area for temperature and gas composition and the results would benefit from tweaks to the gas flow rates.

Kurzfassung

EAF-Staub wird derzeit über Verfahren recycelt, die auf karbothermischer Reduktion beruhen. Die Einführung eines H_2-basierten Reduktionsverfahrens könnte dazu beitragen, die Treibhausgasemissionen zu verringern, sodass die involvierten Unternehmen ihren Beitrag zum europäischen Green Deal leisten können. Obwohl einige Studien bereits die technische Machbarkeit bewiesen haben, muss ein endgültiger Prozess noch gefunden werden. Eine Schlüsselrolle spielt dabei die Reaktionskinetik zwischen den festen Bestanteilen des EAF-Staubs und gasförmigem H_2. In dieser Arbeit wurden die relevanten Reaktionen in thermogravimetrischen Versuchen mit hochreinen $ZnFe_2O_4$- und Fe_2O_3-Pulvern untersucht. Die Ergebnisse aus den Versuchen mit den Reinsubstanzen wurden dann mit Experimenten an reinem EAF-Staub verglichen. Ziel war es, die Kinetik der einzelnen sequenziellen Reduktionsschritte zu untersuchen. Es konnten kinetische Modelle für die einzelnen Reduktionsschritte von $ZnFe_2O_4$ und Fe_2O_3 gefunden werden, während bei den Ergebnissen für Fe_2O_3 einige Unklarheiten bestehen blieben. Die Ergebnisse deuten auf ein unter-schiedliches Verhalten der Eisenoxidreduktion von $ZnFe_2O_4$ und Fe_2O_3 hin. Hauptsächlich unterscheiden sich die ersten beiden Reduktionsschritten bis zum FeO, welche im Fall von $ZnFe_2O_4$ durch Keimbildung und Diffusion begrenzt sind. Die begrenzenden Mechanismen für Fe_2O_3 scheinen Keimbildung und Wachstum zu sein. Der abschließende Reduktionsschritt zu metallischem Fe läuft bei beiden Materialien ähnlich ab und folgt einem geometrischen Kontraktionsmodell. EAF-Staub verhält sich bei der Reduktion ähnlich wie $ZnFe_2O_4$. Eine umfassende kinetische Studie mit besonderem Augenmerk auf EAF-Staub muss jedoch noch durchgeführt werden. In weiterführenden Experimenten sollten dieselben Reaktionen in einem weiteren Parameterbereich für Temperatur und Gaszusammensetzung untersucht werden. Außerdem würden die Ergebnisse von einer Optimierung der Gasflussraten profitieren.

Eidesstattliche Erklärung

Ich erkläre an Eides statt, dass ich die vorliegende Arbeit selbstständig verfasst, andere als die angegebenen Quellen und Hilfsmittel nicht benutzt, und mich auch sonst keiner unerlaubten Hilfsmittel bedient habe.

Ich erkläre, dass ich die Richtlinien des Senats der Montanuniversität Leoben zu „Gute wissenschaftliche Praxis" gelesen, verstanden und befolgt habe.

Weiters erkläre ich, dass die elektronische und gedruckte Version der eingereichten wissenschaftlichen Abschlussarbeit formal und inhaltlich identisch sind.

Affidavit

I declare on oath that I wrote this thesis independently, did not use other than the specified sources and aids, and did not use any unauthorized aids.

I declare that I have read, understood, and complied with the guidelines of the senate of the Montanuniversität Leoben for "Good Scientific Practice".

Furthermore, I declare that the electronic and printed version of the submitted thesis are identical, both, formally and with regard to content.

Felix Hoffel
_____
Vorname Nachname

Leoben, September 2022

Table of Contents

1 Introduction

The recycling of steel scrap in the electric arc furnace (EAF) produces a substantial amount of dust as a by-product. Its composition varies depending on the quality of the scrap and is generally classified as hazardous waste [1]. Zn compounds make up a substantial portion of this dust, especially when the recycled scrap contains galvanized steel. Therefore, EAF dust constitutes an important secondary resource for Zn.

Currently, the state-of-the-art process to recycle EAF dust is the Waelz process. It distils the Zn via carbothermic reduction and collects it as crude zinc oxide after reoxidation. This treatment process generates 500–1000 kg CO_2 per ton of treated EAF dust. As the European Green Deal, requires all industries to reduce greenhouse gas emissions, an alternative recycling process is needed to meet these goals. The reduction with H_2 offers a thermodynamically feasible alternative. Although numerous efforts have already been made to find alternative recycling routes, no economically feasible process has been established industrially to date [2–7].

A key role to find a technologically feasible solution for the large-scale introduction of a novel metallurgical process plays the knowledge of the involved reaction kinetics. To prevent wrong conclusions from insufficient data, extensive studies are necessary for the proper upscaling of a process. As the composition of EAF dust varies, it is desirable to understand the behaviour of its major constituents.

This work aims to investigate the reduction kinetics of pure $ZnFe_2O_4$ which is a major constituent of EAF dust with a focus on the selective reduction of the Fe-oxide in $ZnFe_2O_4$. A comparison with the kinetic behaviour of pure Fe_2O_3 is of particular interest because extensive kinetic data of its reduction with H_2 is present in the literature. Finally, the results are compared to the behaviour of EAF dust during reduction with H_2. The kinetic data is acquired through thermogravimetric analysis.

2 Fundamentals of the EAF Dust Reduction

This section summarises the most important characteristics of EAF dust, its basic reduction behaviour, and the used concepts to evaluate experimental data kinetically.

2.1 Characterisation of EAF dust

Compositions and morphologies of EAF dusts strongly depend on the operational practice of steel mills. The contained components are mainly formed by 3 mechanisms [4]:

- The high temperature in the vicinity of the electric arc vaporizes surrounding compounds having a high vapour pressure
- Bubble bursting from slag foaming caused by the reaction of carbon with the oxides in the slag leads to the ejection of particles
- Fine particles from the charged materials are carried over to the off-gas stream, especially if they are of low density

The main constituents of EAF dust are fine particles which show a high tendency to agglomerate due to their small size and hygroscopic nature. These particles comprise multiple elements present in the different charge materials of the EAF. The batch-wise operation of the EAF additionally results in variations of the off-gas dust over time. This leads to strong inhomogeneity in dust composition. Usually, different particle structures can be identified. Zn-rich phases tend to occur in finer grains while Fe-containing particles are usually larger. Spherical shapes matching the composition of EAF slags are also found in different dust samples. The fine-grained fraction which makes up most of the dust is reported to be in the range of 0.3–3 µm. These fines build dense clusters in the range of 10-200 µm. [1, 8–10]

The EAF dust composition depends on the charged materials, which is why its chemical composition varies strongly. Table 1 lists common ranges of the elements found in EAF dust. Also, F can be found to some extent [11]. The origin of the steel scrap particularly influences the Zn-content as well as that of other volatile metals. Na, K, and Cl are mainly introduced with coal, polymer coatings, or in the form of salts [12]. The amount and type of slag additives used in the steel mill also influence their content in the dust.
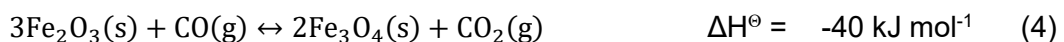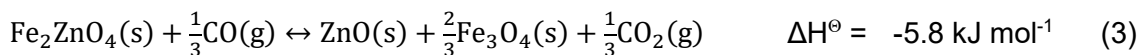
Table 1: Ranges for element concentration found in EAF dust [1, 8, 10, 12, 13]

	element concentration [mass-%]																
	Fe	Zn	Mn	Pb	Cr	Cu	Si	Ca	Mg	Na	K	Cl	Cd	C	S	Al	O
min	15	3.7	0.3	0.7	0.2	0.1	1.2	0.9	0.4	0.4	0.5	1.9	0.03	0.3	0.1	0.2	bal.
max	48	36	5.9	3.2	0.6	0.3	2.2	5.9	2.8	5.6	3.5	8	0.1	6.4	1.2	2.7	bal.

Most elements are present as oxides, but the presence of Cl, F, and S also leads to the formation of complex solid solutions. Fe and Zn are reported to be mainly present as Fe_3O_4, ZnO, $ZnFe_2O_4$, and ferrite spinel with other elements [8, 9, 11, 12]. Several other phases that were also reported are $ZnCl_2$, ZnF_2, $PbCl_2$, PbF_2, PbO, MnO_2, NaCl, KCl, CaO, MgO, and SiO_2 [8, 9, 11, 13].

2.2 State of the art in EAF dust processing

EAF dust is predominately recycled by carbothermic reduction processes. Its goal is the reduction of ZnO to gaseous Zn according to equation (1). CO is mainly formed via the Boudouard reaction (2) which effectively results in the conversion of ZnO with solid C. This separation of Zn by reduction and selective evaporation takes place in packed or moving bed reactors with a relatively low bed height. Additionally, $ZnFe_2O_4$ decomposes (3), Fe-oxides are reduced (4)–(6), and several volatile compounds (especially chlorides) evaporate. While reducing conditions are present in the bed, an oxidising atmosphere is attained by supplying air to the area above. Gaseous Zn oxidises (7) and fine ZnO dust leaves the reactor with the off-gas as the main product. As a side effect of the reoxidation, the enthalpy of equation (7) is partly used to heat the bed. Other volatile substances in the charged materials contaminate the product which is separated from the gas in bag filters. The Waelz process is the dominating technology for the extraction of Zn from EAF dust. There the described reactions take place in a rotary kiln with the gas flowing in counter current to the bed. EAF dust is mixed with coal/coke and slag building additives before it is charged into the kiln. The addition of CaO is necessary to hinder the formation of liquid phases to reduce sintering effects which would negatively affect the solid-gas reaction. Alternatively, rotary hearth furnaces, find application in the processing of EAF dust. [14–16].
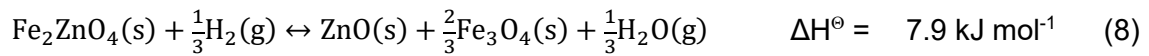
$$ZnO(s) + CO(g) \leftrightarrow Zn(g) + CO_2(g) \qquad \Delta H^\ominus = \ 198 \ \text{kJ mol}^{-1} \qquad (1)$$

$$C(s) + CO_2(g) \leftrightarrow 2CO(g) \qquad \Delta H^\ominus = \ 172 \ \text{kJ mol}^{-1} \qquad (2)$$

$$Fe_2ZnO_4(s) + \tfrac{1}{3}CO(g) \leftrightarrow ZnO(s) + \tfrac{2}{3}Fe_3O_4(s) + \tfrac{1}{3}CO_2(g) \qquad \Delta H^\ominus = \ -5.8 \ \text{kJ mol}^{-1} \qquad (3)$$

$$3Fe_2O_3(s) + CO(g) \leftrightarrow 2Fe_3O_4(s) + CO_2(g) \qquad \Delta H^\ominus = \ -40 \ \text{kJ mol}^{-1} \qquad (4)$$

$$Fe_3O_4(s) + CO(g) \leftrightarrow 3FeO(s) + CO_2(g) \qquad \Delta H^\ominus = \ 37 \ \text{kJ mol}^{-1} \qquad (5)$$

$$FeO(s) + CO(g) \leftrightarrow Fe(s) + CO_2(g) \qquad \Delta H^\ominus = \ -17 \ \text{kJ mol}^{-1} \qquad (6)$$

$$Zn(g) + \tfrac{1}{2}O_2(g) \leftrightarrow ZnO(s) \qquad \Delta H^\ominus = \ -481 \ \text{kJ mol}^{-1} \qquad (7)$$

2.3 Fundamentals of H₂-reduction of EAF dust compounds

The reduction of Zn-and Fe-containing oxides with H_2 proceeds through similar reactions as with CO. The decomposition of $ZnFe_2O_4$ takes place according to equation (8). ZnO reacts with H_2 to form gaseous Zn according to equation (9). Although the standard free energy of the reactions becomes negative only at 1497 K, the reaction is feasible at much lower temperatures for low values of its reaction quotient (10). The Fe-oxides also react in a similar manner according to equations (11)–(13). [17]

The biggest differences compared to the reduction with C are:

- the reducing agent can only be supplied as a gas rather than as a solid reactant
- all the reactions are endothermic, except for equation (11) which becomes exothermic at elevated temperatures
- It is hardly possible to sustain reducing conditions in the bed and oxidizing conditions in the surrounding atmosphere

The relevant reaction steps for the reduction of $ZnFe_2O_4$ with H_2 are listed in equations (8) to (13). For easier readability, equations (8) or (11) are also referred to as the first reduction step in this work. Equally, the second and third reduction step refer to equations (12) and (13). [16]

$$Fe_2ZnO_4(s) + \tfrac{1}{3}H_2(g) \leftrightarrow ZnO(s) + \tfrac{2}{3}Fe_3O_4(s) + \tfrac{1}{3}H_2O(g) \qquad \Delta H^{\ominus} = \quad 7.9 \text{ kJ mol}^{-1} \qquad (8)$$

$$ZnO(s) + H_2(g) \leftrightarrow Zn(g) + H_2O(g) \qquad \Delta H^{\ominus} = \quad 239 \text{ kJ mol}^{-1} \qquad (9)$$

$$Q^{ZnO \rightarrow Zn} = \frac{p_{Zn} * p_{H_2O}}{p_{H_2}} \qquad (10)$$

$$3Fe_2O_3(s) + H_2(g) \leftrightarrow 2Fe_3O_4(s) + H_2O(g) \qquad \Delta H^{\ominus} = \quad 0.7 \text{ kJ mol}^{-1} \quad (11)$$

$$Fe_3O_4(s) + H_2(g) \leftrightarrow 3FeO(s) + H_2O(g) \qquad \Delta H^{\ominus} = \quad 78 \text{ kJ mol}^{-1} \quad (12)$$

$$FeO(s) + H_2(g) \leftrightarrow Fe(s) + H_2O(g) \qquad \Delta H^{\ominus} = \quad 24 \text{ kJ mol}^{-1} \quad (13)$$
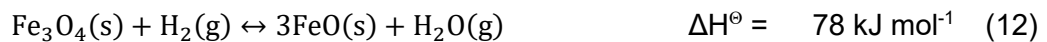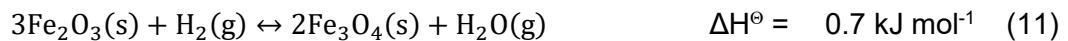
Figure 1 shows the phase diagram of the system Fe-Zn-H-O with a constant Fe/Zn-ratio of 2. The fraction of H_2 in the gas phase is plotted on the x-axis and the temperature on the y-axis. The equilibria in the diagram were calculated with FactSage 8.0 using the factPS, FToxid, and FTmisc databases [16]. The solid black lines represent the equilibrium lines of reactions (12) and (13) in the presence of Zn. Stoichiometric $ZnFe_2O_4$ is only stable at low H_2- partial pressures and temperatures, while Fe^{2+}- and Zn^{2+}- ions are interchangeable in the spinel phase. Therefore, reaction (8) does not directly lead to the formation of two separated phases. The reaction rather proceeds throughout the bounds of the phase stability area. Stoichiometric

$ZnFe_2O_4$ decomposes to ZnO and non-stoichiometric zinc ferrite ($ZnFe_2O_{4,zf}$). With increasing temperature and H_2 concentration, ZnO separates from the spinel while the Fe^{2+} concentration in the spinel increases. The calculations predict a different behaviour at higher H_2 concentrations and low temperatures, where $ZnFe_2O_4$ decomposes more strictly. With increasing temperatures, the spinel phase shows a higher solubility for Zn again. The contour lines in the diagram represent the molar fraction of Fe^{2+} with respect to all divalent metal ions in the spinel. FeO and ZnO are also not present as pure phases. Instead, they are calculated allowing for the dissolution of each other, leading to a Zn-containing wustite (FeO_{zf}) and a Fe-containing zincite ZnO. Additionally, the diagram shows the equilibrium lines for the system Fe-O-H as red dot-dashed lines.
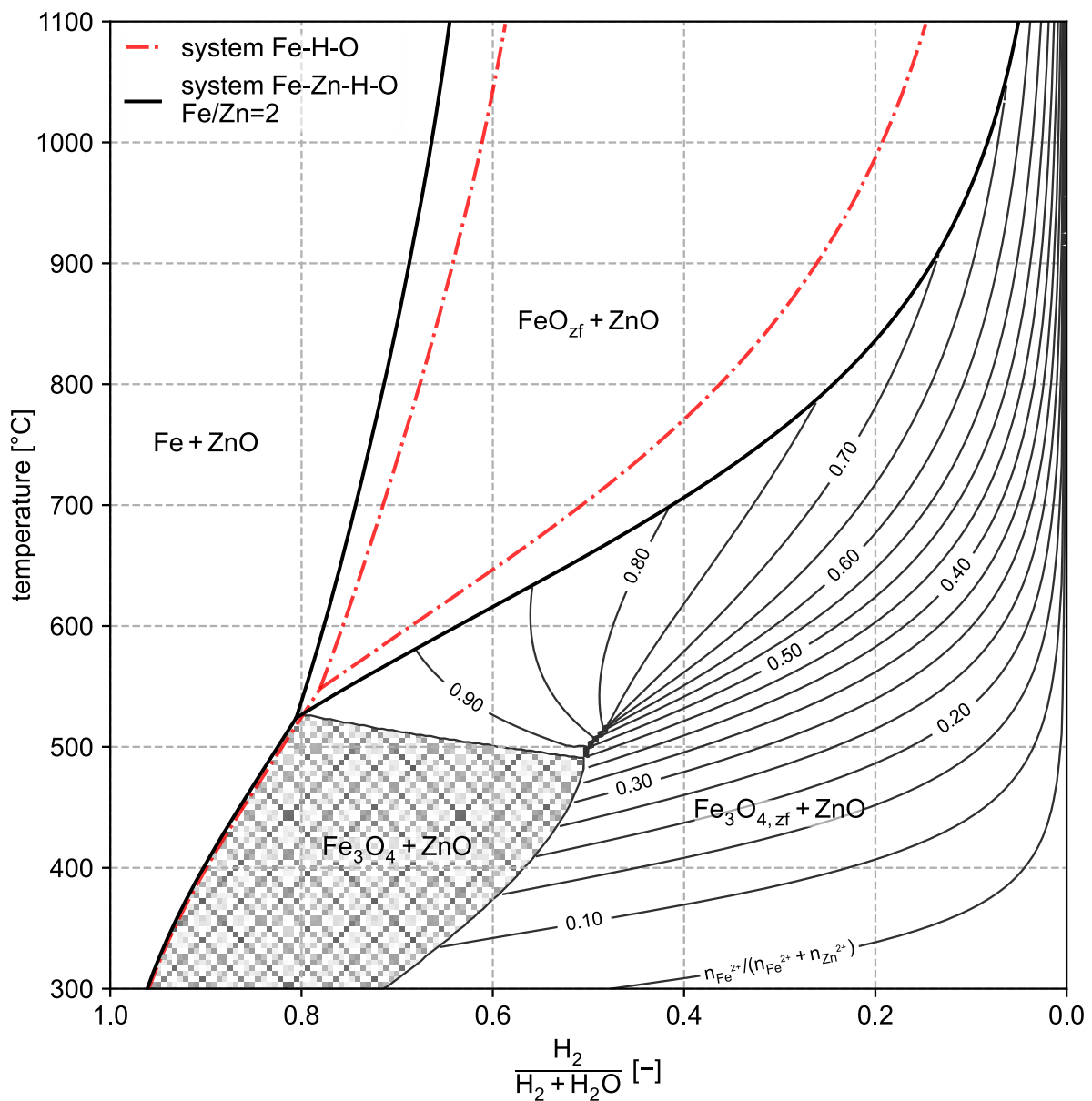
Figure 1: Phase diagram for the system Fe-Zn-H-O with a molar ratio of Fe/Zn=2 [2, 16]

2.4 Kinetics concepts of solid-gas reactions

Once the thermodynamic feasibility of a chemical reaction is verified, evaluating its kinetics is the obvious continuation to transfer the reaction from a laboratory scale to an industrial process. The following chapter presents important fundamental concepts that are used for kinetic modelling. Finally, a detailed view of modelling concepts used for solid-gas reactions is given.

2.4.1 General concepts

The conventional way to describe the progress of a general chemical reaction (14) is to use the molar extent of reaction calculated as of equation (15). While this formulation has the benefit of being valid for all species involved in a single reaction, it is an extensive variable. This concept is particularly useful for dealing with closed systems that host multiple dependent reactions. Another way of describing the extent of a reaction is the fraction conversion (16), which represents an intensive variable. This concept is preferable when dealing with open systems by using the fraction of the limiting reagent to describe the progress of the reaction. With a variable defined for the progress of a reaction, the rate of the reaction is defined as the time derivative of said variable. Equation (17) shows the rate of a reaction for isothermal, isobaric, and homogenous systems. This definition is valid for a reaction, independently of the chosen species. By dividing the rate through the volume of the system, the rate is expressed as an intensive variable. To describe heterogenous reactions it is often appropriate to define the rate regarding the interfacial area, as outlined in equation (18). [18, 19]

$$0 = \sum_i \nu_i \cdot A_i \tag{14}$$

$$\xi = \frac{n_i - n_{i,0}}{\nu_i} \tag{15}$$

$$\alpha = 1 - \frac{n_i}{n_{i,0}} \tag{16}$$

$$r = \frac{1}{V}\frac{d\xi}{dt} \tag{17}$$

$$r_S = \frac{1}{S}\frac{d\xi}{dt} \tag{18}$$

A_i .... species involved in reaction

ν_i .... stoichiometric factor for species i [mol]

ξ .... molar extent of reaction [-]

α .... fraction conversion [-]

n_i .... amount of reactant species i [mol]

$n_{i,0}$ .... amount of reactant species i at start of reaction [mol]

r .... rate of reaction [mol·s^{-1}·m^{-3}]

r_s .... rate of reaction at interface [mol·s^{-1}·m^{-2}]

V .... volume [m^3]

S .... surface area [m^2]

The reaction rate depends on various variables, which originate from different phenomena (e.g., intrinsic reaction, diffusion, reactant transport) that are necessary for the progress of the reactions. Any derived formulation is therefore only valid for the specified operating conditions and its applicability on a different scale cannot be determined beforehand. This necessitates, examining the rates of chemical and physical processes involved in a reaction to derive predictions for possible applications. Possible variables influencing the reaction rate are temperature, pressure, composition, properties of catalysts, geometry, heat transfer, and mass transfer. [18, 19]

$$r = k \cdot \Phi(C_i) \tag{19}$$

$$k = A \cdot e^{-\frac{E_a}{R \cdot T}} \tag{20}$$

$$\Phi(C_i) = \prod_i C_i{}^{\beta_i} \tag{21}$$

k .... rate constant [mol·s^{-1}]

$\Phi(C_i)$ .... function for the dependency on the concentration

C_i .... concentration of reactant i [mol·dm^{-3}]

T .... absolute temperature [K]

β_i .... reaction order [-]

R .... universal gas constant [J·mol^{-1}·K^{-1}]

A .... pre-exponential factor [mol·s^{-1}]

E_a .... activation energy [J·mol^{-1}]

Equation (19) shows the rate law for chemical reactions. It generally decreases monotonically with time for homogenous reaction systems. Coefficient k is called the reaction rate constant and is usually independent of the composition. It depends on the absolute temperature and is expressed in form of the Arrhenius equation (20). Chemical reactions often depend on the concentration of the reactants according to the reaction order model in equation (21). If

reactions in both, the forward and reverse direction of a reaction equation are happening, the net rate of the reaction can be expressed as the difference between the two rates. [18, 19]

For the observation of the kinetics of a reaction, a useful metric needs to be chosen. The experimental results thereby need to be connectable with the reaction rate in a reliable and reproducible way. Various signals may be used, ideally measured continuously in-line to generate a large sample count. Examples are gas composition, sample weight, heat transfer, gas pressure, volume changes, etc. [18–20]

2.4.2 Solid-gas reactions

The kinetics of chemical reactions between solid and gaseous phases is typically described by mathematical models of the time derivative of fraction conversion. Commonly used reaction models are based on mechanistic assumptions or of a purely empirical nature. To describe pyrometallurgical reactions, analogous to equation (19), two separate and independent terms are used. One is the Arrhenius equation as the temperature dependant term and the second term considers the dependency on the fraction conversion. Due to difficulties in separating single intrinsic phenomena, thermal analysis results in composite values dependent on involved physical phenomena. The resulting constants from this approach, as it is depicted in equation (22), are therefore called "apparent" parameters. This may lead to different parameters exhibiting unexpected behaviour. For example, the apparent activation energy may vary with temperature and/or reaction extend. [19–21]

$$\frac{d\alpha}{dt} = k(T) \cdot f(\alpha) \tag{22}$$

$f(\alpha)$ .... model function for the dependency on the fraction conversion

The described model is based on the premise of an existing analytical solution to integrate the rate equation. It is not intended for the implementation of additional parameters and therefore, is limited in its use. Numerous other variables influence the reaction kinetics in an observed system. A few examples are volume, geometry, nucleation conditions, gas composition, specific surface, pore fraction, etc [22]. Extensive studies are necessary to model the overall kinetics of an industrial process based on small-scale experiments.

Numerous reaction models for solid-gas reactions have been derived from mechanistic assumptions. Table 2 lists several of these models in their differential forms grouped by their underlying mechanistic assumptions. [21]

The nucleation and growth model after Johnson, Mehl, Avrami, Erofeyev, and Kolmogorov (JMAEK) assumes the reaction rate to be first limited by the nucleation rate of new grains. Starting locally at lattice defects or geometric features, germ nuclei need to grow up to a certain

size to become stable growth nuclei. The rate of reaction then additionally depends on the growth of these nuclei. Two major limitations work against these purely acceleratory conditions. One is the ingestion of possible nucleation sites by growing nuclei. The second is the coalescence of multiple growing nuclei limits the reaction rate by decreasing the interfacial area between reactants and the products. These assumptions lead to a sigmoidal curve for the fraction conversion with respect to time. [21, 22]

Table 2: Rate expressions for different reaction models [21, 22]

model	$f(\alpha)$
reaction order model	$(1 - \alpha)^n$
geometric contraction	$(1 - \alpha)^{\frac{n-1}{n}}$
Šesták-Berggren	$\alpha^m \cdot (1 - \alpha)^n \cdot (-\ln(1 - \alpha))^p$
nucleation models:	
power law	$n \cdot \alpha^{\frac{n-1}{n}}$
Johnson-Mehl-Avrami-Erofeyev-Kolmogorov	$n \cdot (1 - \alpha) \cdot [-\ln(1 - \alpha)]^{\frac{n-1}{n}}$
diffusion models:	
1-dimensional diffusion	$\dfrac{1}{\alpha}$
2-dimensional diffusion	$-\dfrac{1}{\ln(1 - \alpha)}$
3-dimensional diffusion (Jander)	$\dfrac{3(1 - \alpha)^{\frac{2}{3}}}{2\left[1 - (1 - \alpha)^{\frac{1}{3}}\right]}$
Ginstling-Brounshtein	$\dfrac{3}{2\left[(1 - \alpha)^{-\frac{1}{3}} - 1\right]}$

The geometrical contraction models assume rapid nucleation of a product layer on the surface of crystal particles. Subsequently, the reaction interface progresses towards the centre of the reacting particles. The two possible cases are elongated cylindrical or spherical-shaped particles. These lead to the concepts of a contracting area or a contracting volume. Both models incorporate the size of the particle into the rate constant. Consequently, systems with varying particle size spectra can exhibit a change in their kinetic behaviour. [21, 22]

Solid-state reactions may also occur between different crystal lattices with the reaction front at their interface. When the transport of reactants or products to the interface becomes rate-determining, an appropriate model can be deduced from Fick's first law of diffusion. The varying geometry of the reacting particles leads to different diffusion models. As the diffusion

coefficient is included in the rate constant and usually follows an Arrhenius relation, it superimposes the kinetic parameters for the temperature dependency of the intrinsic reaction. If the reaction rate is proportional to the amount of remaining reactant raised to a particular power, an order-based model may be appropriate. [21, 22]

The reaction model after Šesták and Berggren [22] is an attempt to combine the effect of various mechanisms in a single equation. The single terms in the different models only differ from each other by a variation in the exponents. The application of this model, therefore, allows for a first assumption regarding the involved mechanisms in a relatively simple manner. It is important to keep in mind though, that a good fit of a reaction model onto the data cannot deliver a reliable explanation on its own. Additional investigations are necessary to reach a reliable conclusion (e.g., morphological, chemical, or XRD analysis at different values of fraction conversion).

2.4.3 Mechanisms during gas-solid reactions

The reduction of a piece of ore or an oxidic agglomerate involves a series of consecutive physical and chemical mechanisms. Figure 2 schematically illustrates the involved steps. A solid body is surrounded by a gas stream with constant composition. The first transport step is the diffusion of the gaseous reactant through the adhering boundary layer (I) followed by gas diffusion through macro pores (II). After further diffusion through micro pores (III) the reaction takes place at the gas-solid phase boundary (IV). The reaction involves adsorption of the reducing gas, the oxygen separation as the actual chemical reaction, formation and growth of nuclei, solid diffusion, and the desorption of the product gas. The reactant gas diffuses then outwards through the micro pores (V), macro pores (VI), and the adhering gas layer (VII). [23]
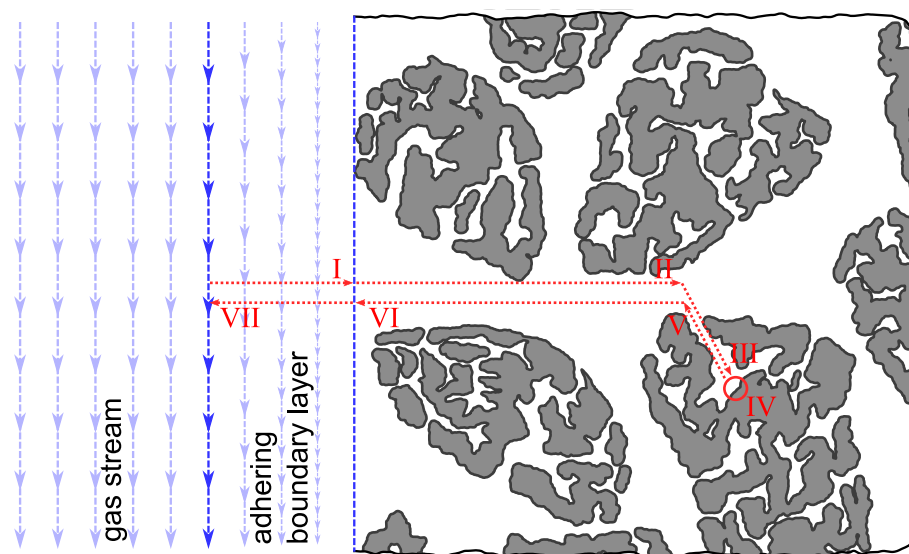
Figure 2: Mechanisms during the solid-gas reduction of oxidic agglomerates [23]

2.4.4 Studies on $ZnFe_2O_4$ and Fe_2O_3

Steel mill dust comprises to a large extent of different Fe-oxides, ZnO, and $ZnFe_2O_4$. The subsequent section summarises relevant kinetic studies, that were performed on similar materials to the ones used in this work. Extensive studies have been conducted on the H_2 reduction of Fe-oxides, while former investigations on EAF dust and $ZnFe_2O_4$ focussed on the carbothermic reduction. Although some research was performed on the H_2 reduction of $ZnFe_2O_4$ not too much data exists, especially on the behaviour of powder samples.

Reduction of $ZnFe_2O_4$

Tong and Hayes investigated the reduction behaviour of dense $ZnFe_2O_4$ under H_2 and H_2/N_2 atmosphere. They used cube-shaped samples with a length of 1 mm in isothermal experiments in the range of 500–1000 °C. The experiments were interrupted at varying progress to evaluate the samples to obtain kinetic data. They additionally investigated the reaction front on polished samples using scanning electron microscopy – quantising the chemical composition via EDX. For pure $ZnFe_2O_4$ they found that the reaction proceeds in two steps – first the rapid reduction to FeO_{zf} followed by the slower reduction to metallic Fe. The FeO_{zf} phase was shown to build up as a dense layer around the unreacted core, while Fe was predominantly formed as a porous layer. The results of their kinetic study indicate that the reaction is controlled by gas diffusion through the porous Fe layer. Low H_2 partial pressures and intermediate temperatures made the exception, where Fe formed as a dense layer accompanied by poor reduction kinetics. They further investigated the influence of Al_2O_3, MnO, MgO, and CaO impurities in the $ZnFe_2O_4$ phase. CaO increased the reaction rate for their experiments while the other additions had an adverse effect. [24]

An investigation on the selective reduction of 2 g samples made from $ZnFe_2O_4$ powder with 1 l·min^{-1} H_2 was performed by Kazemi and Du Sichen. The setup consisted of isothermal thermogravimetric experiments in a temperature range of 623–873 K. The objective was to reduce the samples to metallic Fe and ZnO. Their findings indicate that the reduction rate is partly controlled by gas diffusion inside the material. [25]

Reduction of Fe-oxides

Pineau et al. extensively studied the reduction behaviour of Fe_2O_3 in the temperature range from 220–680 °C. They used a fine-grained raw material with a specific surface of 0.51 m^2·g^{-1}. The reduction was performed with different mixtures of H_2 and N_2. Their work included an extensive collection of literature data on the reduction kinetics of Fe_2O_3 with H_2. They found the apparent activation energy for the reduction from Fe_2O_3 to Fe_3O_4 to be 76 kJ·mol^{-1}·K^{-1} for the reduction with pure H_2. When additional gases are introduced into the gas stream the

apparent activation energy tends to be higher. The literature values in the temperature range of 250–600 °C vary around 60–110 $kJ \cdot mol^{-1} \cdot K^{-1}$ under similar overall conditions. The best fitting kinetic model was determined in-between the 2-dimensional and 3-dimensional nucleation and growth formulation after JMAEK. [26]

The same team of researchers also studied the reduction behaviour of powdered Fe_3O_4 material which was synthesised by reducing their Fe_2O_3 raw material at 600 °C. It had a surface area of 0.7 $m^2 \cdot g^{-1}$ and the kinetic behaviour was studied in a temperature range of 210–700 °C. Their results suggest the reaction to follow a 2-dimensional nucleation and growth model above 390 °C with an apparent activation energy of 44 $kJ \cdot mol^{-1} \cdot K^{-1}$ above this temperature. In the temperature interval of 390–570 °C, the reaction under a pure H_2 atmosphere is shown to proceed to a mixture of metallic Fe and stoichiometric FeO. While above 570 °C non-stoichiometric FeO seemed present as an intermediate product during the reduction, accompanied by a drop in the apparent activation energy. [27]

3 Experimental Investigations

The objective of the experiments was to investigate the behaviour of EAF dust during its reduction with H_2. The experimental setup was designed around thermogravimetric reduction trials of pure Fe_2O_3 as well as $ZnFe_2O_4$ to compare their behaviour during a reducing treatment with that of EAF dust.

3.1 Thermogravimetric reduction trials

A variety of experiments under isothermal and continuous heating conditions were performed. During the experiments, several problems occurred which led to continuous adaptations of the experimental setup. These problems and their solutions are discussed at a later point together with other limitations of the experimental setup.

3.1.1 Experimental setup

The following description of the setup represents the final design of the experiments. Details may vary for different experiments as several adaptations were made during the trials. These adaptations are discussed in chapter 3.1.3 and significant changes in the setup are discussed for the evaluation of the single experiments.

The reduction experiments were performed in a Linseis STA PT1600. For safety reasons, an overpressure valve is present before the gas flare. This leads to a constant overpressure of 0.15 bar in the furnace chamber. The atmosphere consisted of H_2, H_2O, and N_2. The gas mixing system incorporated an evaporator for the supply of gaseous H_2O. A Flusys pump of the model WADose-Lite-HP regulated the mass flow of water to the evaporator which worked at 170 °C. The desired amounts of N_2 and H_2 were first mixed in a mass flow controller (MFC) before they flew into the evaporator. The gas mixture was transferred from the evaporator to the furnace chamber through a heated duct, which was constantly kept at 190 °C. To prevent the condensation of vapour from the gas before the off-gas duct the flange separating the furnace chamber from the scale was also regulated to a temperature of 80 °C. A constant flow of 100 ml·min^{-1} N_2 was used for the protection of the scale throughout all experiments. The protective gas mixed with the process gas to some extent inside the furnace. Figure 3 shows the schematics of the thermal analyser (TA) setup.

Two different sample holders were used for the reduction trials. Figure 4 (a) depicts the measuring system for simultaneous thermal analysis (STA) that was initially installed. The system was equipped with a pair of type C thermocouples. The reference crucible was filled with inert material with an equivalent mass to that of the sample. Although the differential scanning calorimetry (DSC) signal could provide additional quantitative data, calibrating its

1 furnace
2 specimen holder
3 upper flange
4 lower flange
5 heated transfer line
6 protection gas inlet
7 vaccum pump outlet
8 off-gas outlet
9 scale
10 SiC heating element
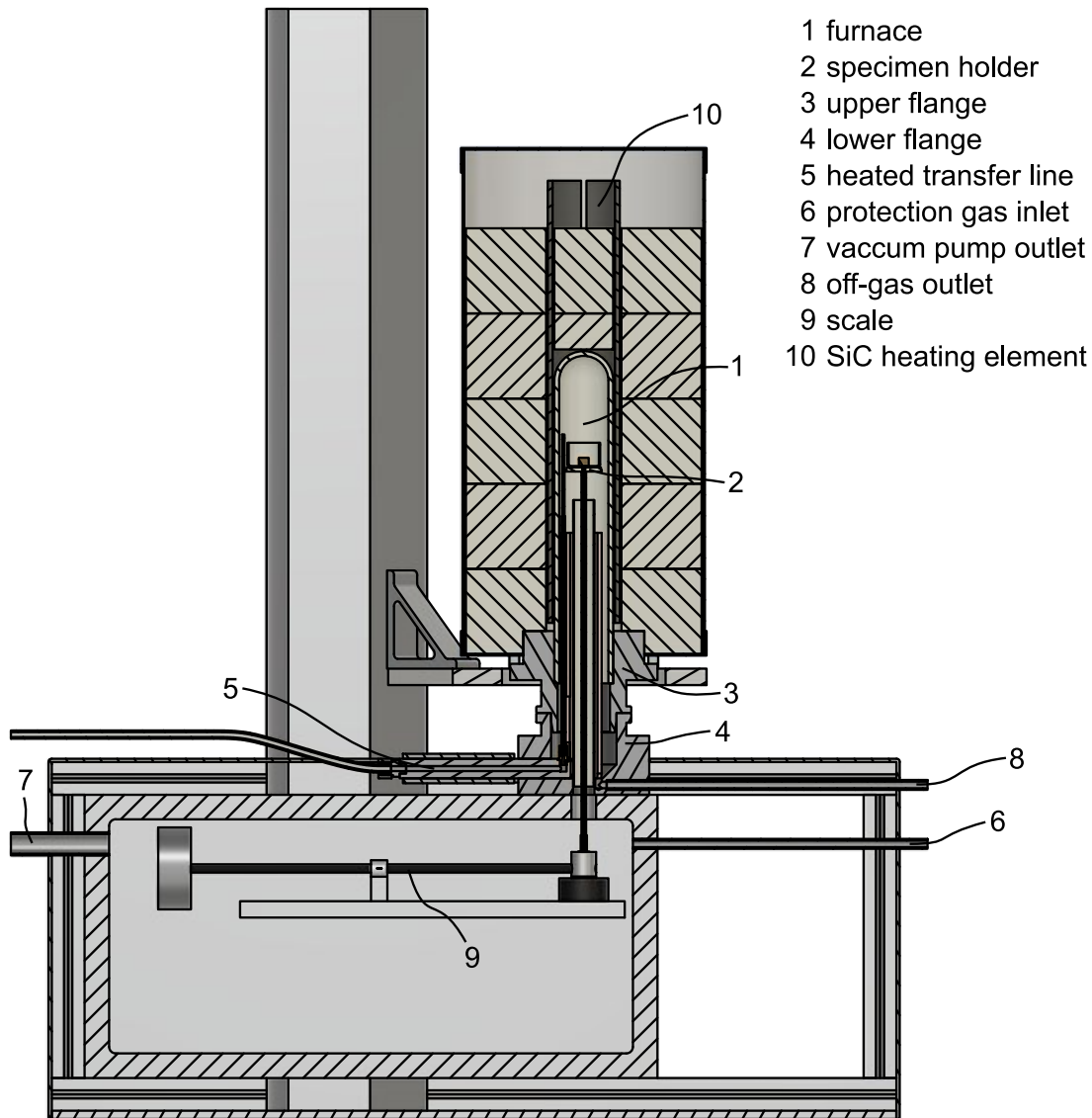
Figure 3: Schematics of TA setup

baseline involves immense additional effort. Therefore, only the mass change signal was used for evaluation. As mass loss curves already provide enough information on investigated phenomena, the required additional effort outweighs the possible benefit. The geometry of these crucibles is dictated by the requirements of a DSC measurement. But the limited pathway for the reaction gases through the relatively small opening does not represent the reaction conditions in upscaled variants of any possible treatment processes. The sample holder was changed to a different system, as fixed-bed or fluidized-bed reactors would be reasonable choices for the solid-state reduction of EAF dust. A specimen holder for thermogravimetric analysis (TGA) was therefore used for most experiments. Compact samples pressed into a cylindrical shape were used. The samples were placed inside a crucible of 20 mm diameter and 15 mm height to provide a better flow of the process gases around the sample. Figure 4 (b) shows the schematics of the sample holder platform which had a type K thermocouple installed and the crucible placed on top.
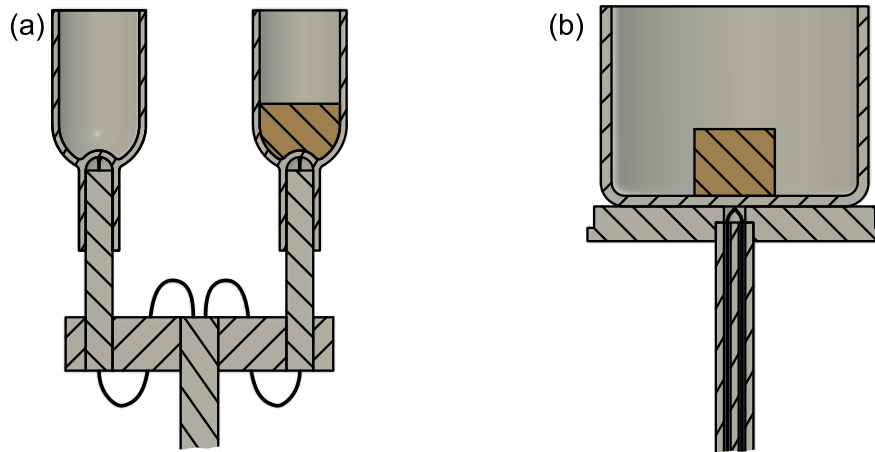
Figure 4: Specimen holders used during experiments, as set up for STA (a) and TGA (b) experiments

A true-to-scale sketch of the furnace chamber with a TGA specimen holder is illustrated in Figure 5. Reaction gas enters the upper chamber through a capillary and protective gas flows from the scale compartment into the furnace via a cylindrical sheath. While the protective gas undoubtedly mixes with the reaction gas during experiments with an STA specimen holder, the platform of the TGA setup separates the two gas streams to some extent. The protection gas also enters the furnace at a lower temperature compared to the reaction gas.

1 sample
2 TGA crucible
3 specimen holder
4 furnace tube
5 thermocouple
6 reaction gas inlet
7 protective gas inlet
8 Cu condensator
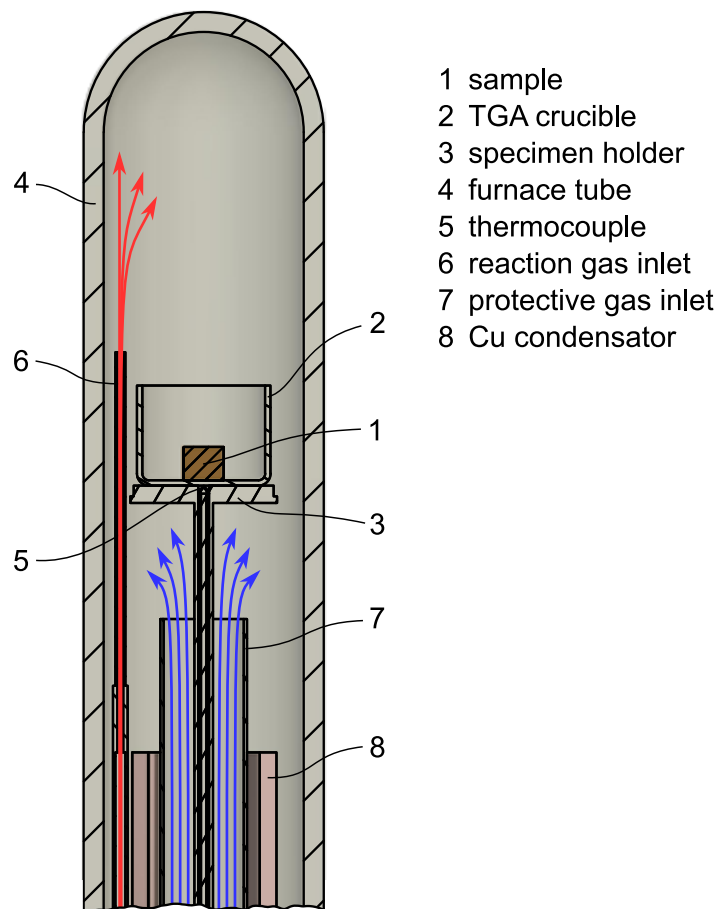
Figure 5: Schematics of the reaction chamber

15

All gases exit through the bottom of the furnace tube outside the inner sheath. The Cu sheath provides a path to conduct heat out of the furnace. The relatively colder surface acts as a condensation trap for material in the gas stream that evaporated from the sample at elevated temperatures.

3.1.2 Sample material and preparation

Three different sample materials were used. Fe_2O_3 was sourced as a powder of 98 % purity from Alpha Aeser (Product No.: 12375). $ZnFe_2O_4$ of 99.6 % purity came from Thermo Fisher (Product No.: 19407). The EAF dust was obtained from a local steel mill. Its chemical composition is depicted in Table 3.

The raw materials were used as loose particles inside a crucible and as pressed tablets. Figure 6 shows the pressed cylinders of the three different sample materials used in the experiments. The sample weight varied in the range of 100–600 mg. Initial trials on the Fe_2O_3 raw material show a mass loss of 3.5 % at 900 °C in the N_2 atmosphere. This mass loss is consistent with a larger batch of sample material, that was calcined under oxidising conditions in air. $ZnFe_2O_4$ showed a mass loss of 3.2 weight-% under the same conditions. Although these values are higher than the stated amounts of impurities, they most probably are related to contents of physically and chemically bound water.
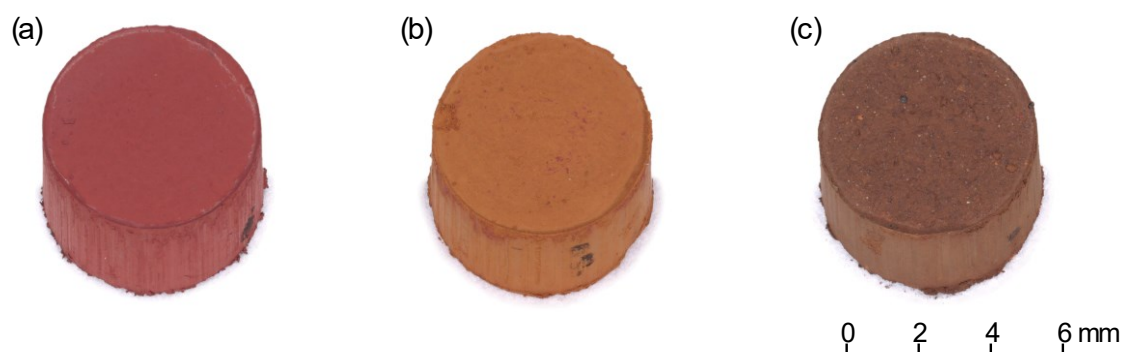
Figure 6: Pressed sample cylinders of Fe_2O_3 (a), $ZnFe_2O_4$ (b), EAF dust (c)

During calcination, EAF dust lost 13 weight-% due to the evaporation of volatile compounds. All raw materials used for the experiments were burned at 900 °C for 3h in air. The tablets were formed into a cylindrical shape in a press die under a uniaxial pressure of 35 $N \cdot mm^{-2}$. Figure 7 depicts the schematics of the press die used to form the tablets. The dies for 300 mg and 600 mg tablets had 6 mm and 7.5 mm diameters respectively. The sample dimensions were chosen in a way that both sample sizes had the same diameter/height ratio. This led to a ratio between the surface areas of the two different cylinders of 1.56. The longer top plunger was used to eject the finished sample cylinders from the dies. The sample cylinders had

enough strength to be manipulated with tweezers and to keep their shape throughout the reduction trials.
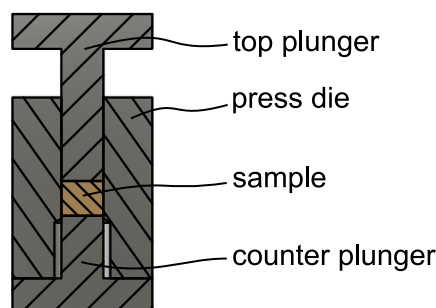
Figure 7: Schematics of press die for the cylindrical tablets

3.1.3 Problems and limitations of the setup with feasible solutions

The thermogravimetric analyser was initially designed to be used with an H_2 atmosphere. The necessary safety precautions for the use of H_2 led to several problems in conjunction with the usage of H_2O vapour in the furnace atmosphere. The investigation of steel mill dust introduced additional problems as a consequence of the high volatility of its constituents.

While using hydrogen in any enclosed reactor it is important to assure that there is no possibility of ingress of oxygen from the surrounding air. Therefore, an overpressure valve is placed at the end of the off-gas duct. This guarantees a constant overpressure in addition to the existing pressure drop resulting from the flow resistance of the reactor. Therefore, all investigations in the TGA took place at an absolute pressure of approximately 115 kPa with a minimal deviation depending on the atmospheric pressure variation. The pressure drop in the off-gas tract also leads to a slight increase in the pressure at the reaction site, which additionally varies with the gas flow rate. The reaction rate of systems involving gaseous reactants is expected to depend on the applied pressure. But these small variations are assumed to have no significant impact on the comparability of single experiments. But it is important to note that comparing results from reaction systems with different absolute pressures in the reaction zone should be done carefully.

To assure a gas-tight seal between the metal flange and the inner alumina tube of the furnace chamber, the flange incorporates a water-cooling loop. This cooling loop was initially regulated to 20 °C, which led to the condensation of water in the flange area. As the flange is in the direct vicinity of the reaction zone, a controlled gas atmosphere cannot be ensured, if water condensates. The problem was only noticed with longer-lasting trials as small amounts of water already evaporated during the cooling under N_2 atmosphere. The problem was solved by increasing the flange temperature to 80 °C. At this temperature, the vapour pressure of water is at 47 kPa [28], which was not exceeded during any experiment.

Zn has a boiling point of 907 °C [16] and several other constituents of EAF dust have even lower boiling points. Thus, they evaporate under the conditions present during the reduction experiments. As the gas travels towards the off-gas duct the evaporated compounds condensate on cold surfaces. Material introduced into the system may then evaporate at a later point interfering with subsequent experiments. During the first experiments with $ZnFe_2O_4$ condensation of Zn on the stem of the specimen holder was observed. This also became evident by irregularities in the mass signal during the experiments. As a countermeasure, a Cu-tube reaching partly into the furnace was placed on the lower flange instead of a formerly present alumina sheath. This focused the condensation onto the Cu surface and allowed the removal of the condensate between experiments.

Blank measurements to calibrate weight changes resulting from gas flow phenomena were conducted and applied where it was possible. However, a large part of the experiments aimed toward breaking down overall reduction reactions into their single consecutive reaction steps. No corrective measures were taken for these experiments. With a sample size of 300 mg and temperature ranges of only a few hundred K for single reaction steps, these deviations were kept at an insignificant level.

The used setup was designed for a maximum flow rate of 35 $cm^3_N \cdot min^{-1}$ for H_2O. For experiments with higher sample weight, this led to a starvation of the gaseous reactant during fast reaction rates. The requirement of controlled partial pressure ratios for H_2 and H_2O did not allow any measures to be taken against this limitation. It was however considered during evaluation and discussion.

3.2 Material characterization

Complementary to the thermogravimetric experiments, the EAF dust was analysed for its chemical composition. Additionally, the specific surface area was determined for all used sample materials.

Chemical analysis

The chemical analysis of the raw material and the reduced samples was determined by EDX on a scanning electron microscope from JOEL of the type JSM-IT300. The installed EDS detector was an Oxford Instruments X-Max[N] 50. The powdered samples were put onto Al sample holder stubs using adhesive conductive carbon tabs. Three measurements were performed for every sample with each measurement scanning a square area of 2x2 mm. The chemical analysis was then calculated as the mean of the three analyses. It should be noted tough, that uneven surfaces are not ideal for the quantitative evaluation of chemical analysis by EDS [29]. Especially elements with low atomic mass tend to be underrepresented when

they are present next to heavier ones. The evaluation of the chemical analysis in this work is complementary to the thermogravimetric experiments and the quantitative precision is sufficient for this purpose. Table 3 shows the chemical analysis of the raw and calcined EAF dust as well as the composition of two reduced samples with 80 and 100 % conversion. The calcination causes the evaporation of Zn, Pb, K and Cl which are present in a variety of compounds.

Table 3: Chemical analysis of raw, burnt, and reduced EAF dust samples

| | weight-% | | | | | | | | | | | | |
	Fe	Zn	Pb	Ca	Mg	Si	Al	K	Mn	Cr	Cu	Cl	O
raw	16.3	46.4	2.8	1.3	0.5	1.1	0.7	1.7	1.2	0.3	0.8	5.4	bal.
calcined	22.6	45.4	-	1.8	0.7	1.3	0.7	0.1	1.8	0.3	0.4	-	bal.
reduced sample nr. 1	59.0	0.5	-	7.3	4.1	4.5	2.4	0.3	5.2	0.8	0.8	-	bal.
reduced sample nr. 2	56.6	7.9	-	6.3	3.0	3.8	1.8	0.3	4.6	0.8	0.8	-	bal.

Specific surface area

The specific surface of the samples was determined by N_2 adsorption at liquid nitrogen temperature. The measurements were performed on a Quantachrome NOVA 2000e. The BET (Brunauer, Emmett and Teller) surface area was determined using the corresponding software. The specific surface of pressed 300 mg specimens for various materials was analysed. Table 4 shows the results of these measurements. The specific surface of Fe_2O_3 and $ZnFe_2O_4$ is comparable, and the calcined materials do not differ outside of the repeat accuracy. The specific surface is higher for non-calcined EAF dust and significantly reduces during calcination of the EAF dust. The difference between calcined and raw EAF dust is most likely caused by the presence of low melting phases.

Table 4: Results of the BET measurements for the sample materials

	specific surface [$m^2 \cdot g^{-1}$]	
$ZnFe_2O_4$	calcined, 900 °C 3h	3.51
	raw	3.49
Fe_2O_3	calcined, 900 °C 3h	3.95
	raw	3.86
EAF dust	calcined, 900 °C 3h	1.01
	raw	5.98

3.3 Experimental procedure and methods for the evaluation

The data resulting from the reduction trials were mass loss-time pairs. This chapter discusses the experimental procedure for individual trials and all further processing performed on the raw data to depict derived relations in their intended manner.

3.3.1 Procedure for individual trials

The samples were weighed directly inside the respective crucibles. Special care was taken, to prevent any ingress of unwanted material in and onto the crucibles which could alter the mass loss in any way. As the sample mass of the tablets was determined only after pressing, they were prepared to an accuracy of ±5 mg. During individual trials, the desired reactions were initiated by changing the furnace temperature or the flow rates of H_2 and H_2O. Experiments were performed either isothermally or under continuous heating. The rapid change of the gas constituents introduces an uncertainty in the gas composition during the initial stage of reactions, as the gas composition present in the furnace needs some time to adapt to the changing composition at the inlet. This factor has a decreasing influence with increasing temperature due to the accompanying increase of the gas velocity. The low reaction time of the H_2O gas flow also does not allow for the simultaneous start of H_2 and H_2O flows. Therefore, continuous heating programs were used whenever possible. For all experiments, the sum of the flows of H_2 and H_2O was 70 $cm^3_N \cdot min^{-1}$, unless otherwise specified for a particular experiment. This value was chosen to achieve an H_2/H_2O ratio of 1 with an upper limit for the H_2O gas flow of 35 $cm^3_N \cdot min^{-1}$. No measurements were performed to correct buoyancy-related effects, as expected deviations in the used setup are negligible and they would be accompanied by an enormous additional effort. After finishing the desired reduction processes, the samples were cooled to room temperature in an N_2 atmosphere. For the kinetic evaluation, experiments for consecutive reactions were summarized into single trials where possible. This seemed reasonable beforehand, as the influence of the earlier reduction history on the kinetic of latter reduction reactions during step-wise reduction was expected to be negligible. Especially the relatively small temperature windows of only 150−250 K for the select reaction led to this assumption. In retrospect, the results have shown that this assumption was not justified, especially in the case of Fe_2O_3.

3.3.2 Data processing for comparative evaluations

Noise in the recorded experimental data is a major problem encountered during the evaluation – especially since the time derivative of the mass loss is of major interest to depict the reaction rate of the investigated reduction processes. Differentiation amplifies signal noise, therefore, smoothing operations were performed on all plotted data for better assessability. A Butterworth

low pass filter was applied using the scipy.signal library in a Python environment [30]. The first-order filter was tuned to an appropriate cut-off frequency, that does not skew any curve features relevant to underlying chemical reactions. The filter was applied twice, once in the forward and once in the backward direction, to the data to counter any phase shift resulting from its application – resulting in a second order filter.

Calculation of the gas composition inside the furnace during the reaction is performed assuming infinitely fast mixing of the reactor gas. The gas atmosphere is calculated as shown in equation (23) equivalently to a continuous stirred tank reactor [18]. Although the purge gas enters the furnace chamber at a different spot than the reaction gas, they were assumed to form one homogenous gas mixture. As long as only Fe-oxides are reduced, all weight loss during a trial can be attributed to O reacting with H_2 during the consecutive reaction steps. As all gas streams from the MFCs are defined at standard temperature and pressure (STP) conditions, the input, as well as the output streams, are adjusted for the reaction conditions treating them as ideal gasses. The temperature was measured at the sample holder and the system pressure of 1.15 bar was applied. The inner gas volume of the furnace was calculated using a computer-aided-design model considering all components present inside of the furnace resulting in 70 cm^3.

$$\frac{dC_{i,f}}{dt} = \left(C_{i,in} - C_{i,f}\right)\frac{\dot{V}_{in}}{V_R} + r_{i,f}$$

(23)

$C_{i,f}$ .... concentration of component i in the reactor

$C_{i,in}$ .... concentration of component i at the inlet

$\dot{V}_{in}$ .... volume stream at input

V_R .... volume of the reactor

$r_{i,f}$ .... reaction rate of component i in the reactor

3.3.3 Data processing for the kinetic evaluations

The kinetic evaluation is selectively performed on the single reaction steps representing equations (8) – (9). For this purpose, the reduction trials were carried out in the stability areas of the targeted product phases, which are depicted in Figure 1. The raw data was cut into the timeframes for the single reactions by hand. This was done, as the onsets and runouts of the reactions varied from very sharp to fluent transitions throughout the experiments. For the last reduction step to metallic Fe during the trials using $ZnFe_2O_4$, a significant part of the mass loss rate was contributed by the reduction of ZnO. These trials were conducted to a point, where the reaction rate would reach a final constant value. This observed constant rate was extracted from the data. The mass loss due to the ZnO reaction was then subtracted from the overall mass loss data. The fraction conversion was calculated for the reaction according to

equation (16) and the first derivative with respect to time was calculated from the mass change. No smoothing operation was performed on the data beforehand. The data was then truncated to an interval of 0.05–0.95 for the fraction conversion. A kinetic model based on equation (24) was then fitted onto the data consisting of the triplet mass loss rate, temperature, and fraction conversion. These data triplets were collected from several experiments spanning over a certain variation of parameters temperature and fraction conversion. The nonlinear parameter fit was performed using the curve_fit function from scipy.optimize library in Python [30]. An appropriate model function f(α) was determined by trial and error from the functions discussed in chapter 2.4.2.

$$\frac{d\Delta m}{dt} = A \cdot e^{-\frac{E_a}{R \cdot T}} \cdot f(\alpha) \tag{24}$$

4 Results and Discussion

As a first step, several trials were performed to determine the reduction behaviour of Fe_2O_3 and $ZnFe_2O_4$ and to compare the influence of basic process parameters. Another objective of these experiments was to define the experimental design for the kinetic evaluation and to find limiting conditions which have to be considered. Lastly, TGA experiments on EAF dust were conducted to compare its behaviour to that of $ZnFe_2O_4$. Therefore, this section is divided into three major parts: the discussion of the comparative experiments, the kinetic evaluation, and the reduction behaviour of EAF dust. Figure 8 depicts the three different sample materials after their complete conversion. The Fe_2O_3 specimens sintered to compact cylinders that shrunk mainly radially. $ZnFe_2O_4$ stayed compact enough to be still manipulated with tweezers after reduction at the higher end of the temperature range. Samples that were reduced at lower temperatures crumbled easily and had virtually no compressive strength. Figure 8 (c) shows an EAF dust sample, which had barely enough strength to be manipulated. The $ZnFe_2O_4$ and the EAF dust sample shrunk equally in radius and height. The loss of strength of these two materials is probably a consequence of the evaporation of Zn during the reduction of ZnO. It should be noted that the used EAF dust sample has an exceptionally high ZnO content. The poor strength of the samples after reduction would be a significant problem in any industrial process. Unfortunately, experimental limitations prevented extending the temperature range further in the scope of this study, to counter this problem.

(a) (b) (c)

0 2 4 6 mm
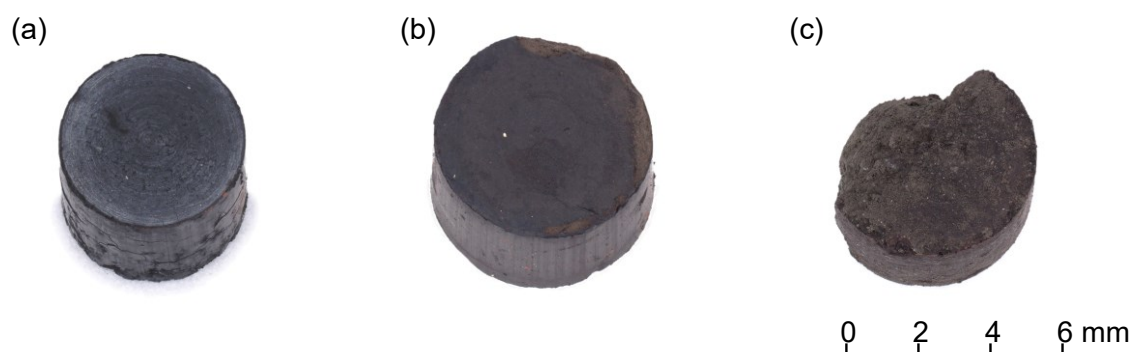
Figure 8: Samples after complete reduction, Fe2O3 (a), ZnFe2O4 (b), EAF dust (c)

4.1 Comparative evaluation of experiments

The results of a series of experiments under variation of the sample mass in STA crucibles can be seen in Figure 9. Due to the nature of the crucible geometry, this leads to a de facto variation in material height while the progress of the reaction border is restricted to the z-axis. These trials were performed with a constant heating rate of 10 $K \cdot min^{-1}$ under 70 $cm^3_N \cdot min^{-1}$ pure H_2 flow. The top part of the figure shows the relative mass loss for the different samples and the two horizontal dashed lines represent the theoretical weight loss to Fe_3O_4 and Fe

23

respectively. For these first experiments, the sample material was not calcined beforehand. Therefore, the actual mass loss does not correlate with the theoretical mass loss. This was solved with a calcination pre-treatment of the sample material, which led to a perfect match of the theoretical and measured mass loss. The reaction rate for this first step increases as the absolute mass increases. A higher sample mass also shifts the maximum reaction rate to a higher temperature. While this indicates that the gas transport influences the reaction to some extent, at least one other mechanism also limits the observed reaction rate. The further reduction to Fe shows only a slight increase in reaction rate with large sample masses and shifts the reactions overall to higher temperatures. This indicates that gas diffusion in the sample may play a significant role under the given conditions. The gas flow rate was the same for all experiments and not adjusted to the mass of the individual samples. Additional experiments with an adjusted specific gas flow rate should be conducted to make a more reliable assertion.
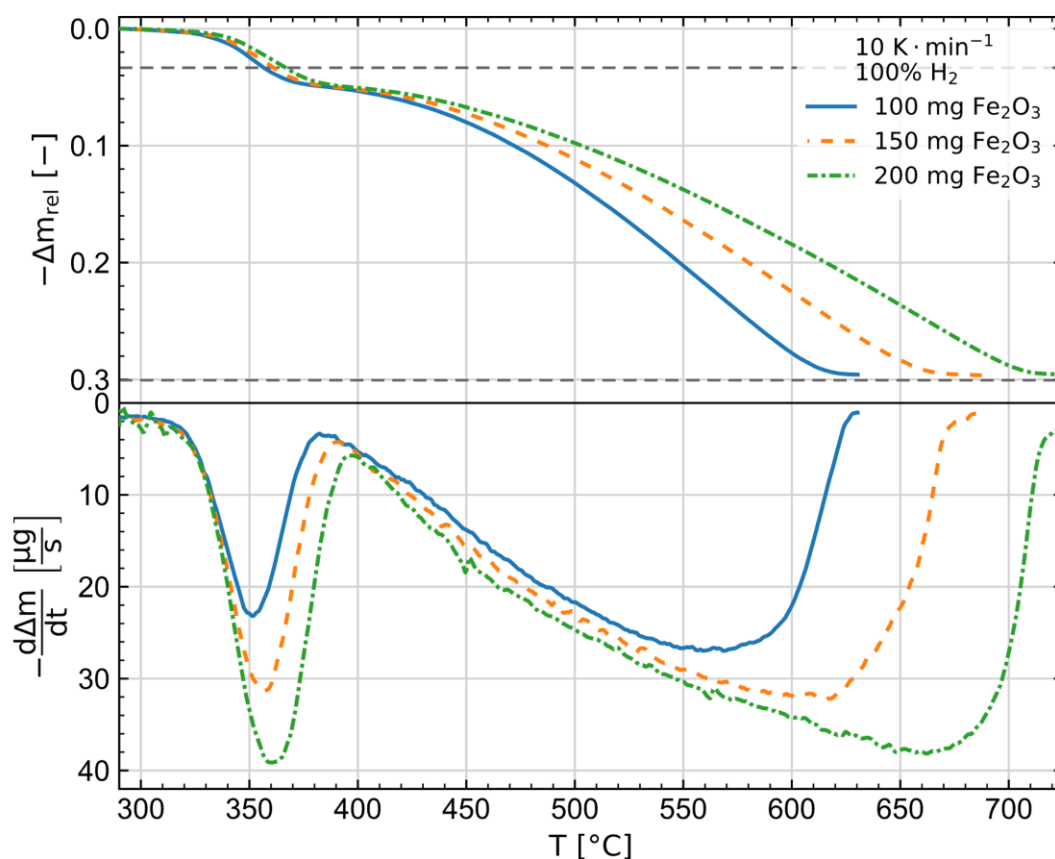
Figure 9: Comparison of samples of different mass in STA crucibles

To further investigate the influence of the sample size, additional experiments with a TGA sample holder were performed. The results for the reduction from Fe_2O_3 to Fe_3O_4 are depicted in Figures 10 and 11. The experiments included the reduction of a single 600 mg sample, two 300 mg samples in the same crucible, and a single 300 mg sample. The gas mixture consisted of equal parts H_2 and H_2O. Additionally, trials with a 300 mg and a 600 mg sample were

performed with an H_2/H_2O ratio of 1.5 for the stepwise reduction to FeO and at a ratio of 9 for the reduction to metallic Fe. All continuous heating experiments were performed with a heating rate of 20 K·min^{-1} and the reduction to Fe was observed at 800 °C. The total gas flow of H_2 and H_2O under STP conditions sums up to 70 cm^3_N·min^{-1} with an additional 130 cm^3_N·min^{-1} of N_2 in the mixture.
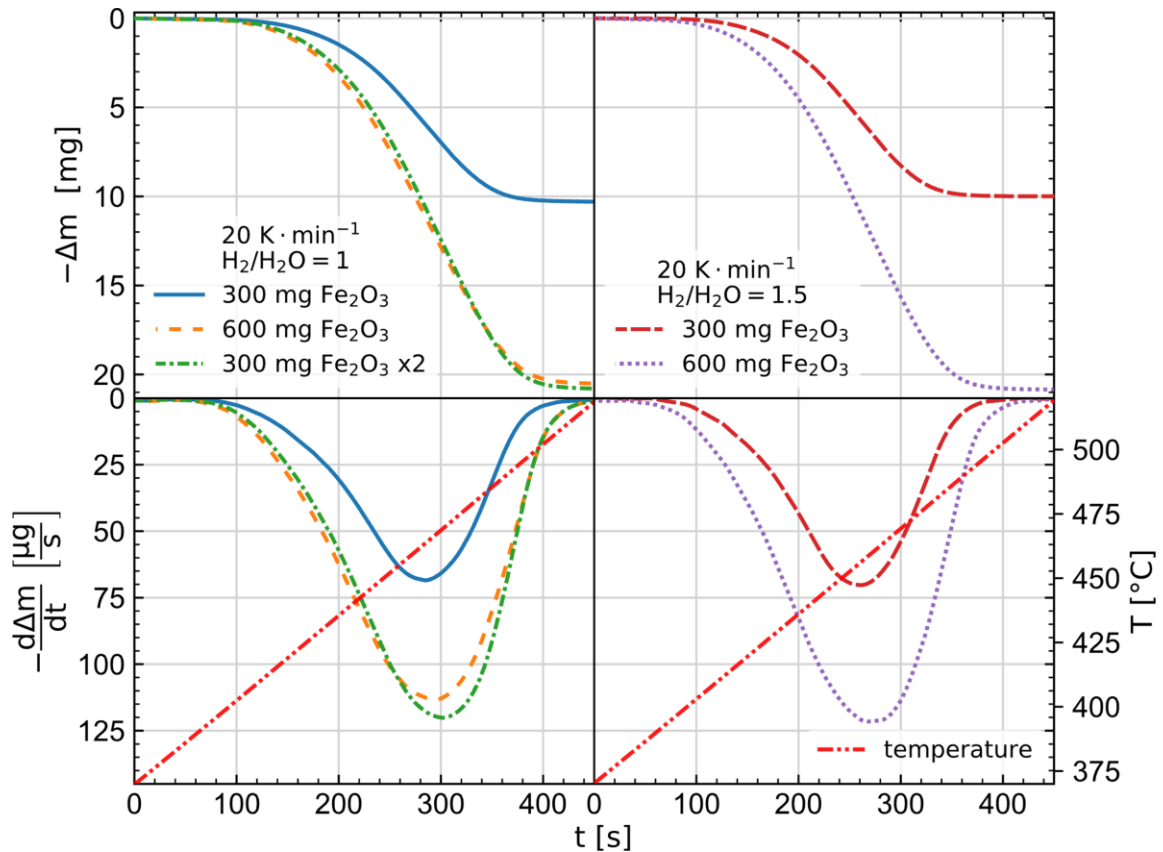
Figure 10: Comparison of the reduction from Fe_2O_3 to Fe_3O_4 for sample tablets with different mass at H_2/H_2O-ratios of 1 and 1.5

The left part of Figure 10 shows that there is almost no difference between a single 600 mg sample and two 300 mg samples for the reduction from Fe_2O_3 to Fe_3O_4. Compared to one 300 mg sample the 600 mg sample shows a lower specific reaction rate and therefore, a slight shift to higher temperatures. If the reaction rate doubles for a sample with twice the mass but only 1.56 times the surface area, the reaction is probably controlled by a phenomenon at the reaction site or by micro pore diffusion. While transport effects in the macro pores or the adhering gas layer can only increase the rate by a factor equal to the ratio of the surfaces of two different samples. In the observed case the rate increases by a factor of 1.76, which indicates mixed controlled kinetics. Again, the gas flow rate was not adjusted to the varying mass during the experiments, which should be investigated further.

Compared to the results at an H_2/H_2O ratio of 1.5 the rate of reaction seems slightly higher for the reaction with higher H_2 contents, and it is also evident, that the reaction is shifted to about

10 K lower temperatures. Additionally, the results in Figure 9 show the reaction happening at significantly lower temperatures in a pure H_2 atmosphere. Although that sample material was not calcined before the experiments and the used setup differs, which makes them not directly comparable. Nonetheless, it is evident, that the H_2/H_2O gas ratio influences the reaction rate of this first reduction step. This is not surprising, since collision theory predicts higher rates with increasing reactant concentration.

The left part of Figure 11 shows the comparison of different-sized samples for the second reduction step from Fe_3O_4 to FeO with an H_2/H_2O ratio of 1.5. The reduction rate seems to be influenced by gas transport as the increase in reaction rate does not equate to the increase in sample mass. The maximum rate is in this case towards a 20 K higher temperature. The rate increase almost matches the increase in cylinder surface area (factor 1.56), which suggests that the rate is partly controlled by gas diffusion through the adhering boundary layer or the macro pores inside the sample.
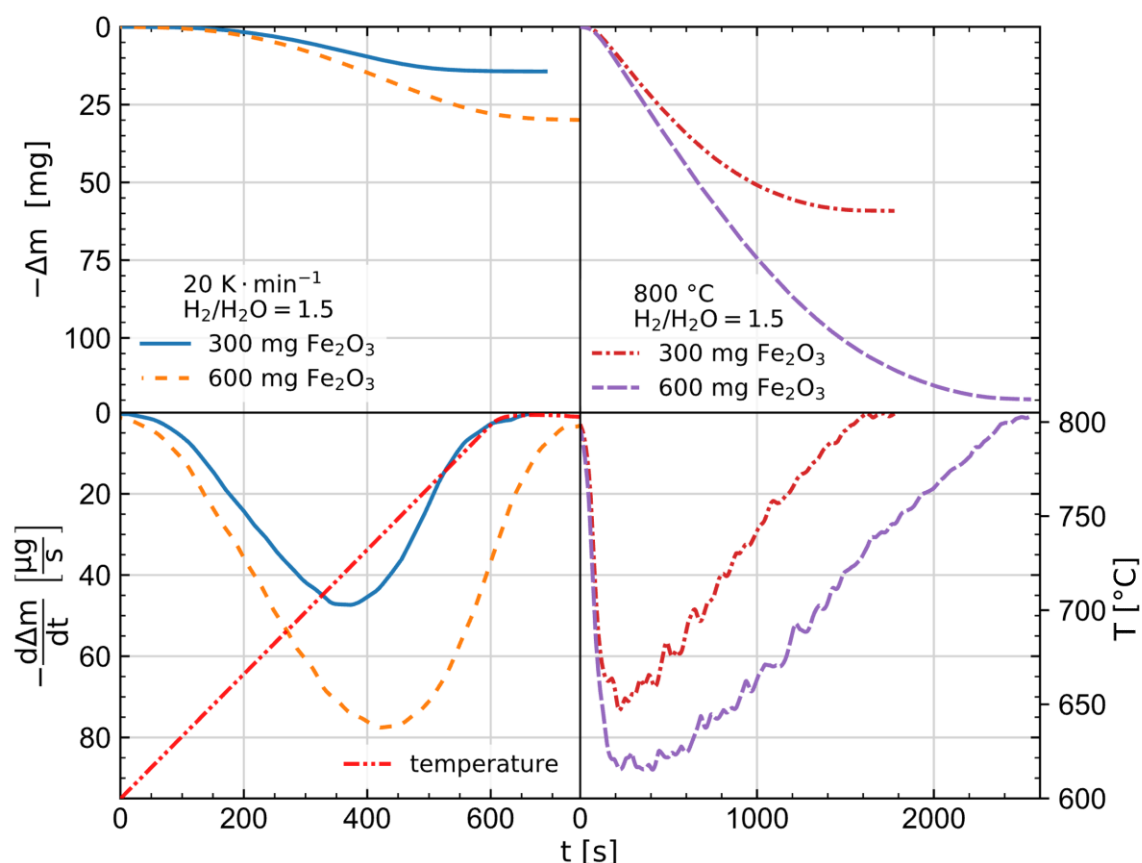
Figure 11: Comparison of the reduction steps to FeO and Fe for sample tablets with different mass

The third reduction step from FeO to metallic Fe was performed under isothermal conditions. Except for a transient initiation phase, the reduction follows a strictly declaratory trend for both samples. The maximum rate of the larger sample increases by a factor of 1.25. A ratio lower than 1.56 was not expected, for any rate controlling mechanism from the adhering gas layer

inwards. Gas starvation in the bulk is the most likely reason for this behaviour. Additionally, the two samples are reduced at slightly different temperatures until they reach this last reduction step which may lead to differences in their morphology. While this may also contribute to the observed behaviour, it is not likely to have a significant influence in this case.

To further investigate the influence of the gas atmosphere, the theoretical change in gas composition inside of the furnace was calculated for the experiment on 600 mg Fe_2O_3. The path of the gas ratio along the time axis is plotted in Figure 12. The plot additionally contains the thermodynamic limit for the occurring reactions calculated from the reaction temperature.
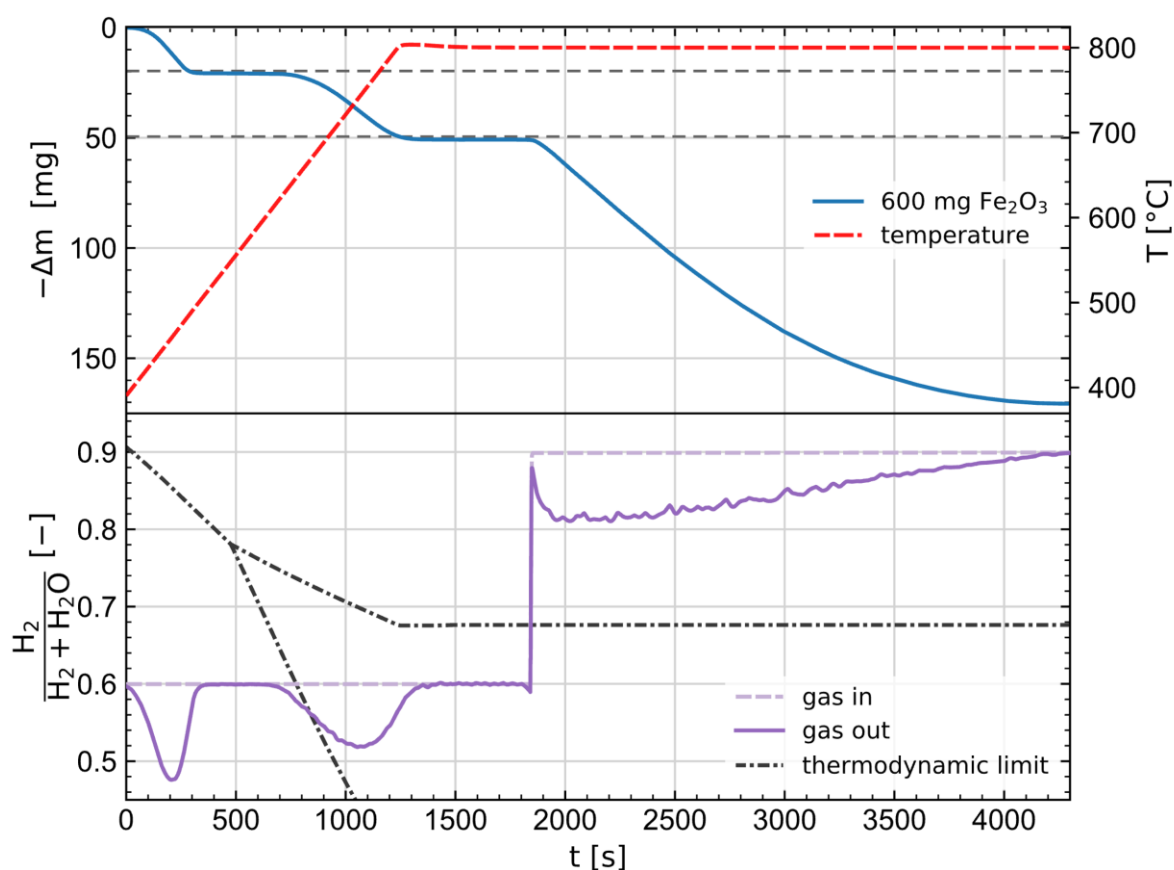
Figure 12: Mass loss of reduction trial on Fe_2O_3 with calculated gas ratios and thermodynamic limits

The results of the experiment on 600 mg were chosen for this depiction because they exhibit relatively large reaction rates. Mass loss rates of 120 µg·s^{-1} were not exceeded during any experiments presented in this work. It should be noted that the heating rate during this trial was set to 20 K·min^{-1} and although the uniform standard for most trails was set to a mass of 300 mg, similar rate values were reached during trials employing the maximum heating rate of 40 K·min^{-1}. The plot shows a large shift in the H_2/H_2O ratio for all reduction steps. This reaction of the first step already becomes thermodynamically feasible at very low ratios of H_2/H_2O. The formerly presented results for different-sized samples indicate, that the present shift in gas composition in this case only leads to minor effects due to gas starvation. For the reduction to

FeO it is visible that the reaction starts at a slightly lower temperature than expected. Although the H_2/H_2O ratio stays well above the thermodynamic limit during most of the reaction it also exhibits a shift in gas composition. Effects due to gas starvation cannot be ruled out for this reaction at this point. A large shift can also be seen for the last reduction step to metallic Fe. In this case, it cannot be ruled out, that the shift present in the gas composition also influences the reaction rate. Although it would be advisable to run the reduction trials at higher gas flow rates, limitations in the experimental setup would not allow for this. Generally, the shifting gas composition distorts the results of single experiments as the gas composition influences the reaction kinetics according to the collision theory.

<u>Investigation of discrepancy between thermodynamic limit and observed data</u>
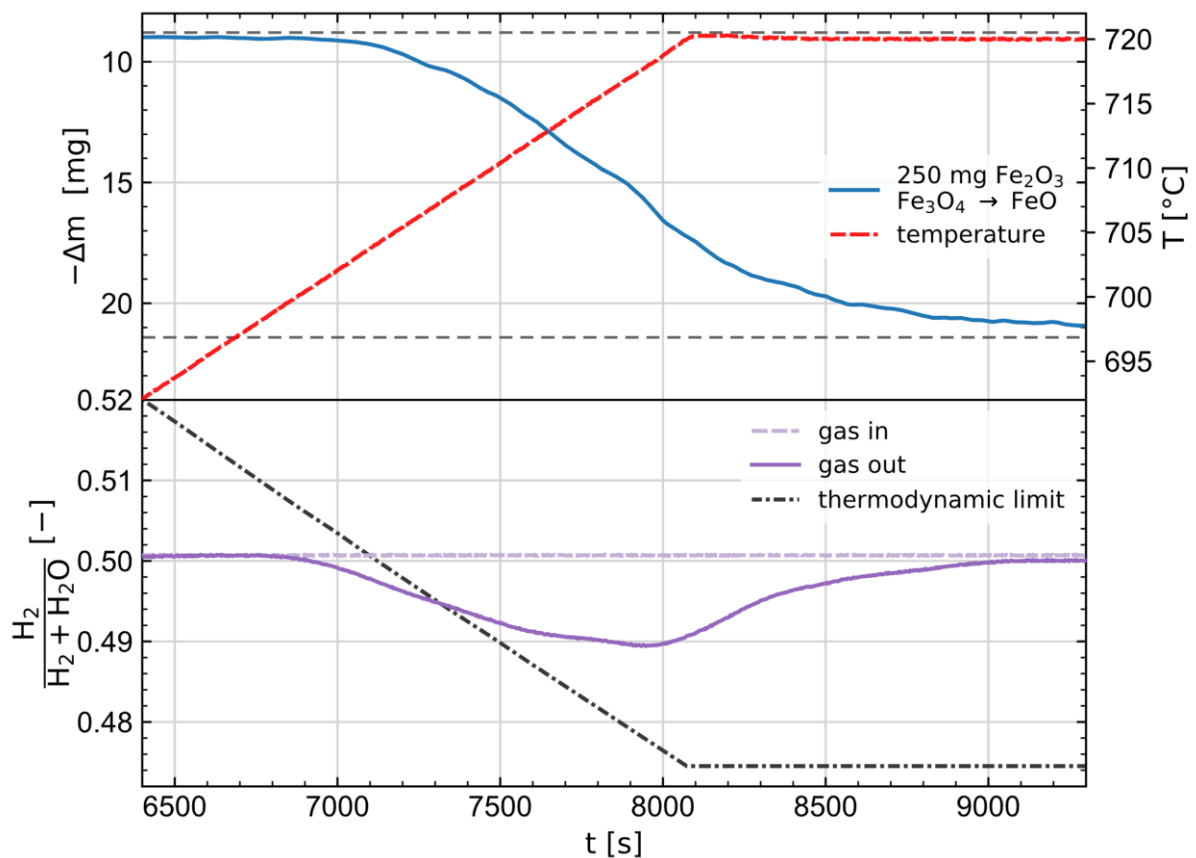
Figure 13: Validation of gas composition on the phase border from Fe_3O_4 to FeO

The discrepancy between the start of the reaction and the thermodynamic limit for the reduction to FeO was further investigated. Figure 13 shows the mass loss curve and the gas composition for the second reduction step of a trial with a heating rate of 1 K·min⁻¹. With a ratio of $H_2/H_2O=1$, the reaction is expected to start at 704 °C. It is again visible, that the reaction starts at a lower temperature. The onset sits 5 K lower than expected, which indicates that the targeted and real gas composition vary slightly. This assumption is supported by the fact that the volumetric flow of H_2O is just controlled by the frequency of a calibrated reciprocating pump.

Unfortunately, it was not possible to verify the gas composition analytically. The results of this trial combined with thermodynamic data suggest, that the actual flow of H_2O is 4 % lower than presumed. Other possible reasons for the discrepancy would be an incorrect value for the H_2 flow or faulty temperature measurement. The first of which seems less likely than an error resulting from the pump, while a deviation due to e.g., a poisoned thermocouple cannot be ruled out. As this phenomenon is predictably steady throughout the experiments, there definitely exists a slight constant error. Due to the systematic nature of this error, it does not impact the qualitative results in this work. However, it must be considered if any quantitative results are used elsewhere.

<u>Investigation of the behaviour of $ZnFe_2O_3$ during the reduction to FeO_{zf}</u>

$ZnFe_2O_4$ generally dissociates during the reduction with H_2 according to equation (8). But the products are $Fe_3O_{4,zf}$ and ZnO and show significant interchangeability between Zn^{2+}- and Fe^{2+}-ions. This leads to a vastly different reduction behaviour during all reduction steps compared to Fe_2O_3. Figure 14 depicts the first two reduction steps for a sample of $ZnFe_2O_4$ at a heating rate of 1 $K \cdot min^{-1}$. Compared to the reduction of Fe_2O_3, there is no distinct point where the reaction comes to a halt, before transitioning to the subsequent reduction step.
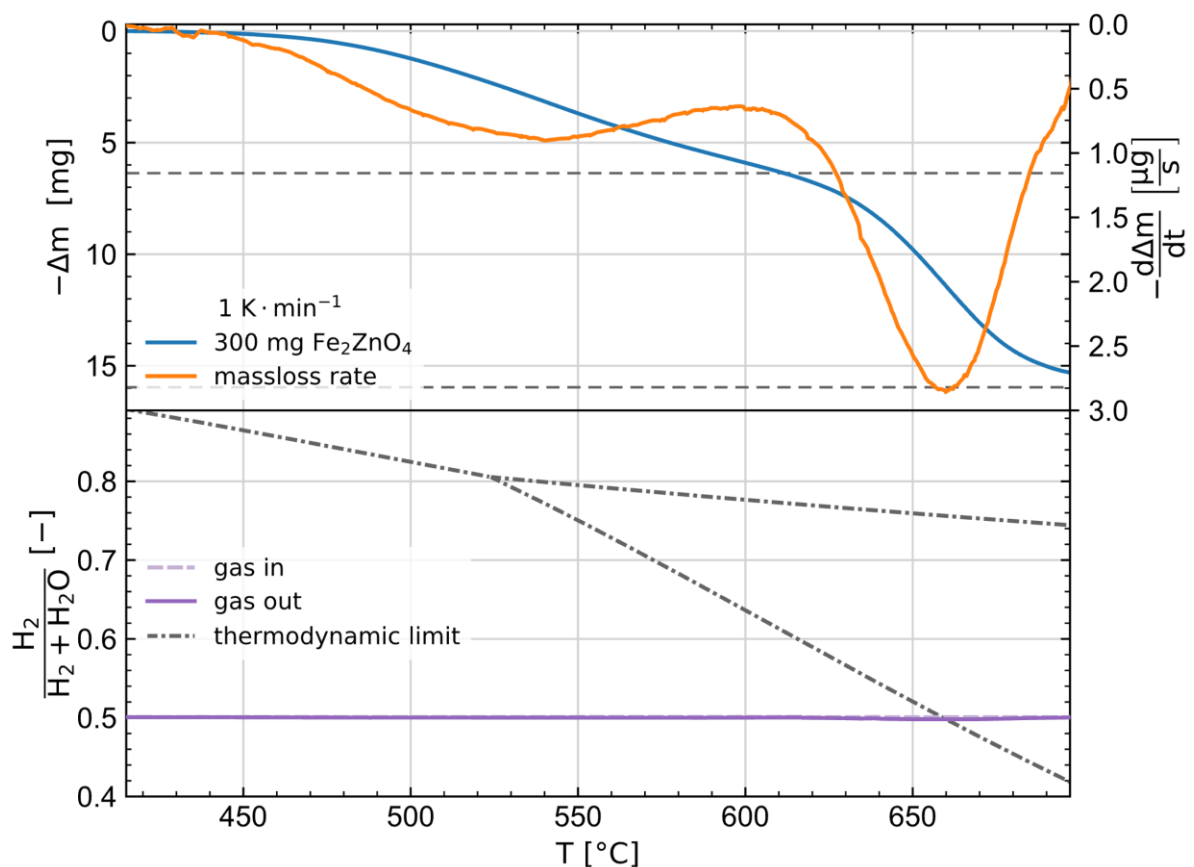
Figure 14: Behaviour of $ZnFe_2O_4$ during slow heating in reducing atmosphere

It should be noted though, that the reaction comes to a halt in experiments that are held isothermally below the equilibrium line of the reaction to FeO_{zf} which can be seen in the lower portion of the picture. The equilibrium compositions of the spinel and zincite phase depend on the temperature, which leads to varying final mass losses for different final temperatures. During further reduction of the spinel phase, the produced FeO shows miscibility with ZnO additionally to its Fe-deficiency. The equilibrium compositions of the various components again are dependent on the temperature and gas composition. Additionally, Figure 14 shows that the reduction does not come to a stop in the stability area for FeO_{zf}, as a constant reduction of ZnO after equation (9) is happening at the present temperatures. The reduction rates of the depicted experiment are relatively low, which is a result of the low heating rate shifting the reactions to lower temperatures. Another reason Is the lower temperature of the phase boundary compared to the reduction of Fe_3O_4. But the reaction also seems to be slowed down by the reactant being a solid solution compared to a pure solid material during the reduction of Fe_2O_3.

Investigation of the onset of ZnO reduction

The reduction of ZnO starts at elevated temperatures and overlaps the reduction reactions of $Fe_3O_{4,zf}$ and FeO_{zf}. It was not possible to find any reasonable measures to avoid it.
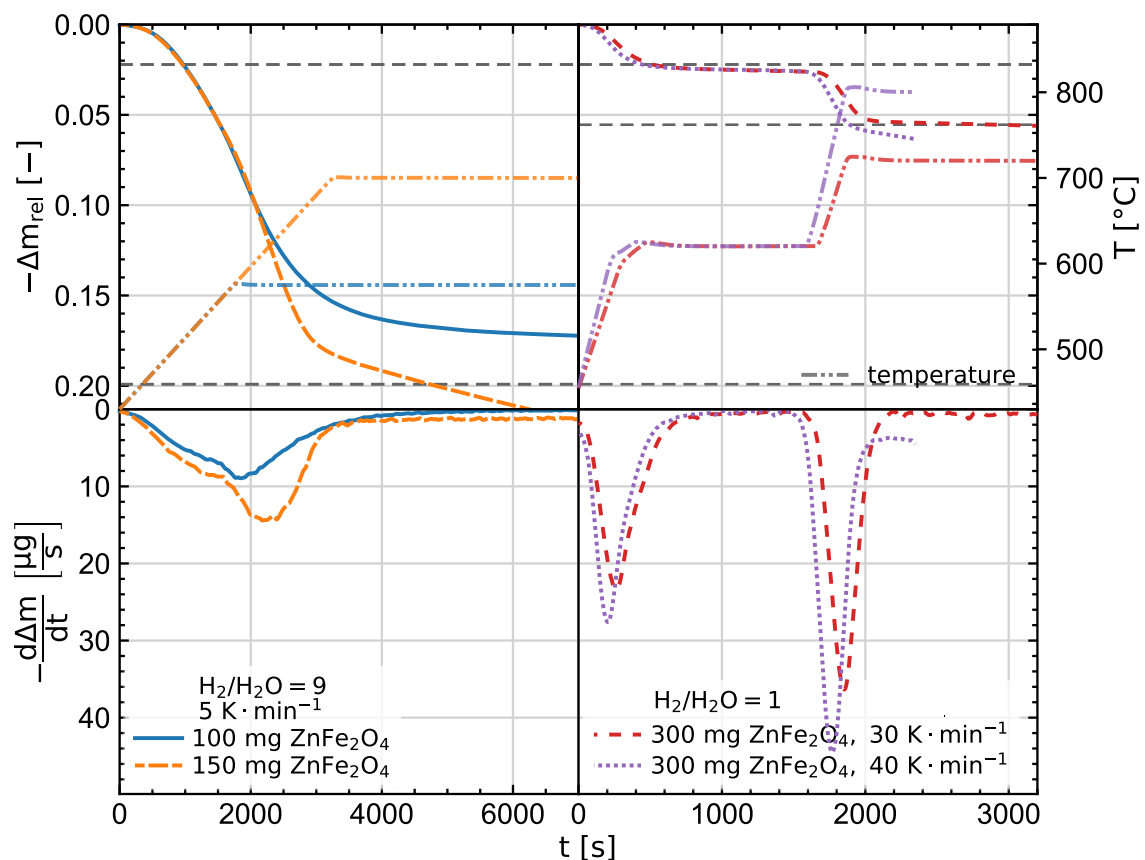
Figure 15: Trials on $ZnFe_2O_4$ to illustrate the boundaries for the kinetic experimental design

Therefore, knowing the magnitude of the ZnO reduction is necessary to establish an experimental design for the selective reduction of $ZnFe_2O_4$. Figure 15 shows the mass loss of four $ZnFe_2O_4$ samples to the point of the total conversion of involved Fe-phases und their respective conditions. The heating rate was 5 K·min^{-1} in both cases. An H_2/H_2O ratio of 9 results in the reduction to metallic Fe in both cases. The dashed lines in the lefthand plot represent the mass loss for total conversion to Fe. With a final temperature of 700 °C a residual mass loss rate can be seen at the end of the trial representing the reduction of ZnO. The sample heated up to 575 °C in the same gas atmosphere does not reach full conversion to Fe, indicating that the ZnO present at this point also contains Fe^{2+}-ions.

At a ratio of $H_2/H_2O=1$, FeO_{zf} and ZnO are present at the mass loss level indicated by the dashed horizontal line. The heating rates during the experiments were 30 and 40 K·min^{-1}. For both final temperatures of 720 °C and 800 °C, a residual reaction rate is visible, indicating the reduction of ZnO. While the reaction rate at 720 °C is relatively low compared to the reduction of the spinel phase, the same cannot be said at a final temperature of 800°C. As the goal of the kinetic evaluation presented in the next section is to break down the overall reduction processes into their single reaction steps, these results have to be corrected for the rate of ZnO reaction.

4.2 Kinetic evaluation

The reduction kinetic of Fe_2O_3 powder was determined to obtain a baseline for the reduction of the Fe-oxides in the used experimental setup. The setup was changed from an STA sample holder to a TGA sample holder during the experiments and a series of trials for the first two reduction steps was performed on Fe_2O_3 before switching to the latter. The first set of trials focused on investigating the first two reduction steps at an H_2/H_2O ratio of 1. An additional set of trials was performed at an H_2/H_2O ratio of 1.5 for the reactions to FeO and 9 for the subsequent reduction to metallic Fe. The experiments on $ZnFe_2O_4$ were performed at an H_2/H_2O ratio of 1 and 9 for the first two and the third reduction steps respectively. A temperature-time program with a constant heating rate was used for the first two reduction steps but was transitioned to an isothermal segment, if further heating would have shifted the system to the equilibrium conditions of a different phase. The applied heating rates were 5, 10, 20, 30, and 40 K·min^{-1}. The reduction to metallic Fe was performed isothermally for all trials.

All plots depicting the single kinetic model fits are arranged similarly. The dotted lines show the actual mass loss rates that were observed in the different experiments. The parameters of the kinetic models are fitted onto these data points. The solid lines represent the predictions for the individual curves, calculated from the kinetic model with the temperature and fraction conversion as the parameters. All curves are plotted either against the temperature or the

31

fraction conversion. Besides for depicting fully isothermal experiments, the latter was chosen, if extended isothermal segments were necessary at the end of a reaction.

Additionally, an Arrhenius plot was drawn for all fitted models. The rate values therefore were divided by the results calculated from the formulation for the dependency on the fraction conversion evaluated for the respective values. Equation (25) shows the resulting formulation rearranged from equation (22) and with equation (20) inserted. The data obtained from this calculation was then plotted against the reciprocal absolute temperature. To preserve clarity in these plots, the data was truncated to 60–80 randomly chosen data points and the points were plotted transparent. The line plotted in every one of these plots is computed from the fitting parameters from the Arrhenius equation.

$$\frac{d\alpha}{dt} \cdot \frac{1}{f(\alpha)} = A \cdot e^{-\frac{E_a}{R \cdot T}} \tag{25}$$

Kinetic evaluation of the first reduction step of $ZnFe_2O_4$ and Fe_2O_3

Figure 16 shows the results for the first reduction step of $ZnFe_2O_4$ in the TGA setup. The model function for the dependency on the fraction conversion is the equation after Šesták and Berggren. The results for model parameters from the fitting operation are m=3, n=0, and p=-4.
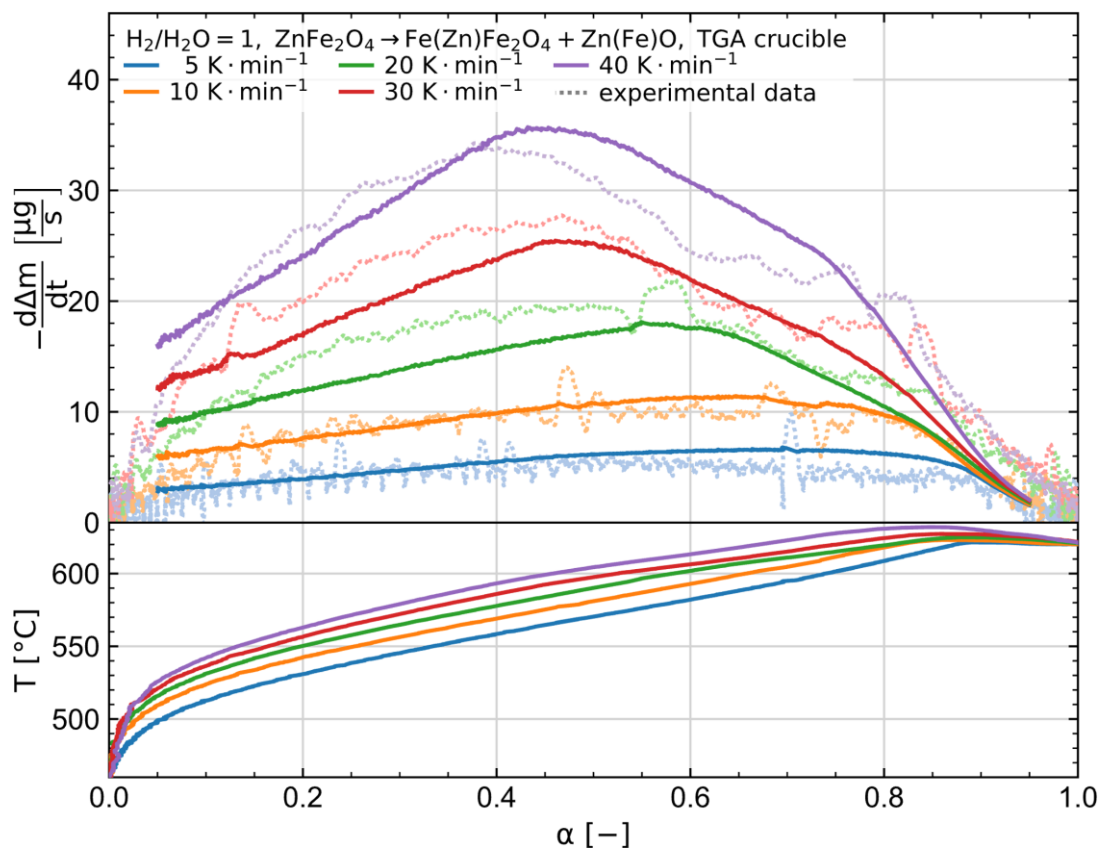
Figure 16: Kinetic evaluation of $ZnFe_2O_4$ reduction in a TGA setup at $H_2/H_2O=1$

The fit seems satisfactory, especially for lower temperatures. While at higher temperatures the beginning of the reaction is slightly underestimated and at the highest heating rate the middle part of the reaction is slightly overestimated. The relatively high value for the parameter of m indicates only a very short acceleratory phase at the beginning of the reaction. For reduction processes in solid-gas systems, a slow rate at the start of a reaction often occurs out of the necessity to introduce cracks into the material to promote gas diffusion. This seems to have only a small influence here as the sample material has a relatively high surface area to begin with. The second relevant part of the formulation is indicative of a rate restriction by diffusion. As the parameter p evaluates to a negative value, this part of the Šesták-Berggren equation is equivalent to the formulation for 2-dimensional diffusion raised to a power. While the higher order of this term cannot be related to any physical transport mechanism, it represents the weighing of the different terms influencing the overall dependency on the fraction conversion. Therefore, the rate also cannot be reliably linked to 2-dimensional diffusion in particular but the results nonetheless indicate a rate limitation by diffusion.

The Arrhenius plot for the first reduction step of $ZnFe_2O_4$ is depicted in Figure 17. The individual experiments follow the fitting parameters very well, indicating that the formulation describes the reaction sufficiently in the given parameter area. The apparent activation energy from the fit is 316 $kJ \cdot mol^{-1} \cdot K^{-1}$.
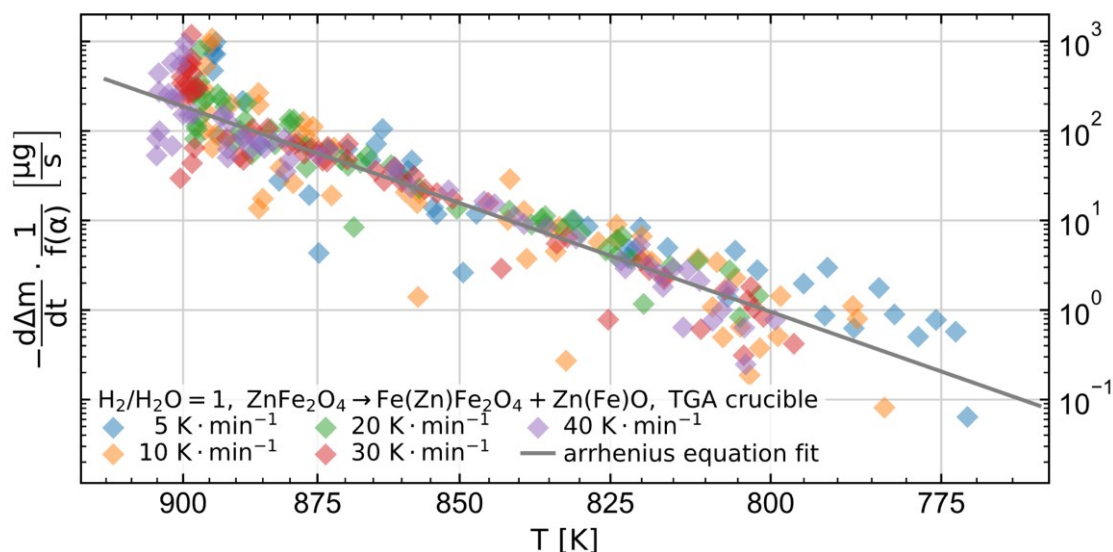
Figure 17: Arrhenius plot for $ZnFe_2O_4$ reduction in a TGA setup at $H_2/H_2O=1$

The results for the reduction of Fe_2O_3 to Fe_3O_4 at an H_2/H_2O ratio of 1 in the TGA setup are shown in Figure 18. The model fit was achieved with a dependency on the fraction conversion after the JMAEK equation with a value for the parameter n of 2. As the plot demonstrates the experimental data show the expected behaviour of a series of experiments performed at varying heating rates. The reactions are shifted towards lower temperatures and the rates vary

33

at similar Temperatures as would be expected for a reaction following a sigmoidal course. The formulation after JMAEK considers a deceleration of the reaction due to geometric limitations and together with the low apparent activation energy the reaction seems chemically controlled rather than by diffusion. In comparison with the rates calculated from the model fit, the calculated reaction rates at low heating rates are slightly overestimated, while they are underestimated at high heating rates.

This Arrhenius plot for these trails is shown in Figure 19. The data of the single experiments deviates visibly from the calculated Arrhenius relation. These results are indicative of a change in the rate-determining mechanism around a temperature of 450 °C. Unfortunately, the data obtained during the experiments is not sufficient to further refine the evaluation in this direction. The value for the apparent activation energy obtained during this fit is 101 kJ·mol^{-1}·K^{-1} and does not fit the investigated system well. Additional experiments are necessary to further clarify the behavioural change at 450 °C.
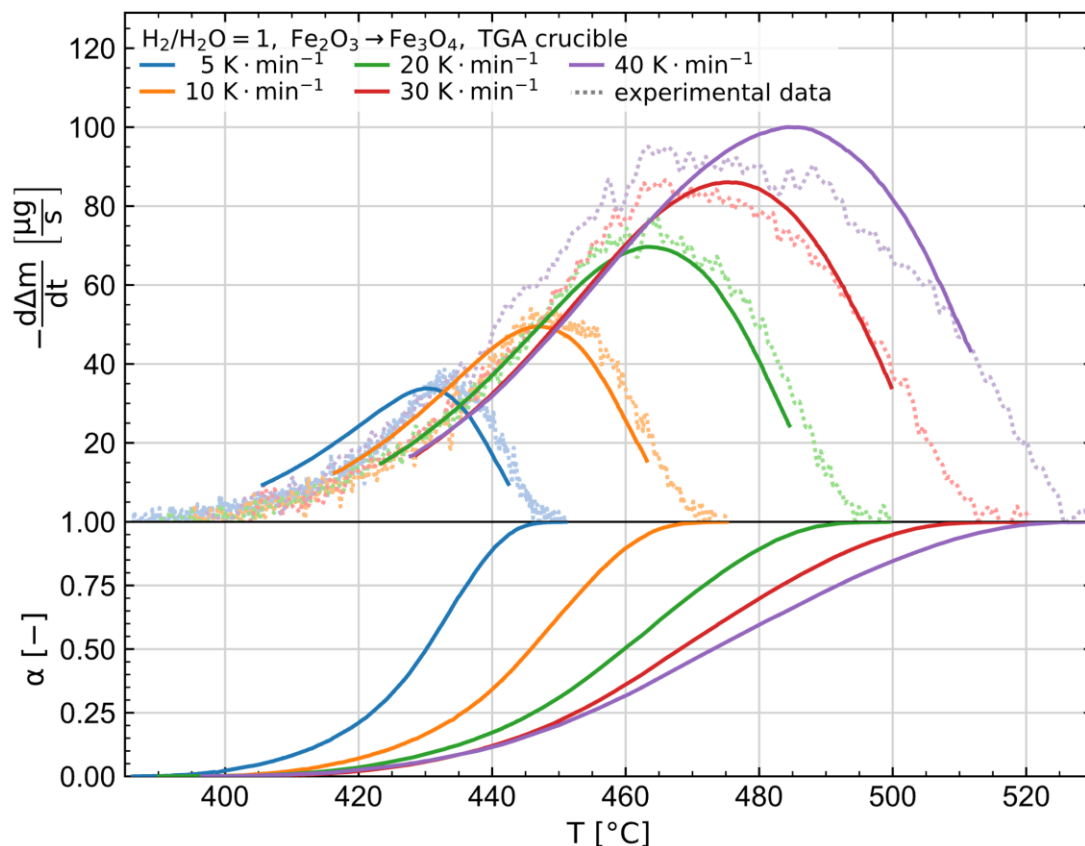
Figure 18: Kinetic evaluation of Fe_2O_3 reduction in a TGA setup at $H_2/H_2O=1$

Considering the reaction of $ZnFe_2O_4$ was evaluated completely above this temperature, its apparent reaction energy is roughly 6 times higher compared to the reduction of Fe_2O_3. Together with the different fit for the model of the fraction conversion dependency, the two compounds act in a vastly different manner during the first reduction step.
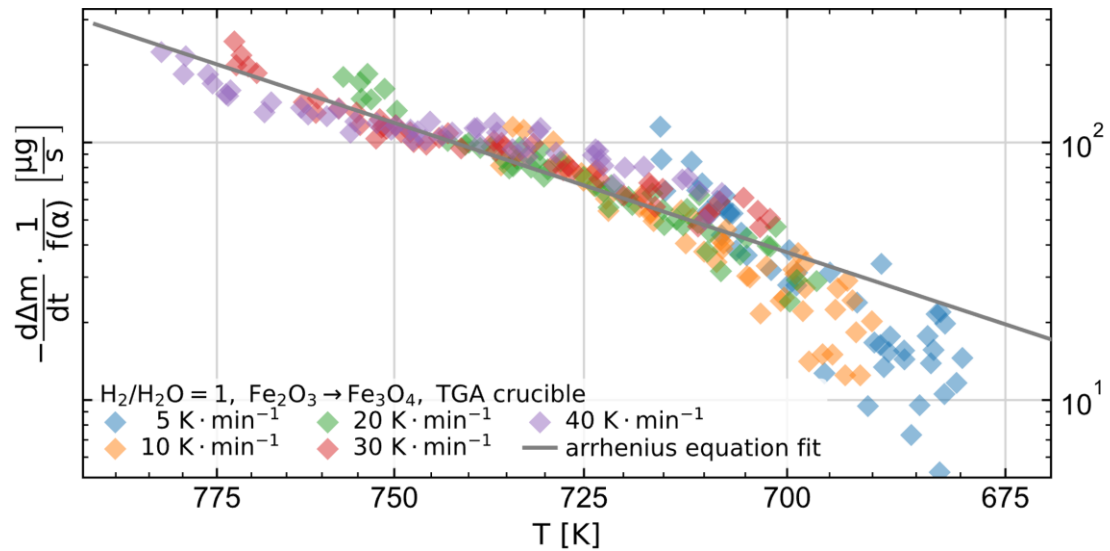
Figure 19: Arrhenius plot for Fe_2O_3 reduction in a TGA setup at $H_2/H_2O=1$

The results for the first step in the TGA setup with a slightly higher H_2/H_2O ratio of 1.5 are shown in Figure 20. The reaction proceeds in the same way as it did at an H_2/H_2O ratio of 1. All reactions are shifted to roughly 10 °C lower temperatures while the reaction rates are also slightly higher. The curves resulting from the parameter fit again indicate that the kinetic model overestimates the reaction rate at low heating rates and underestimates it at high ones.
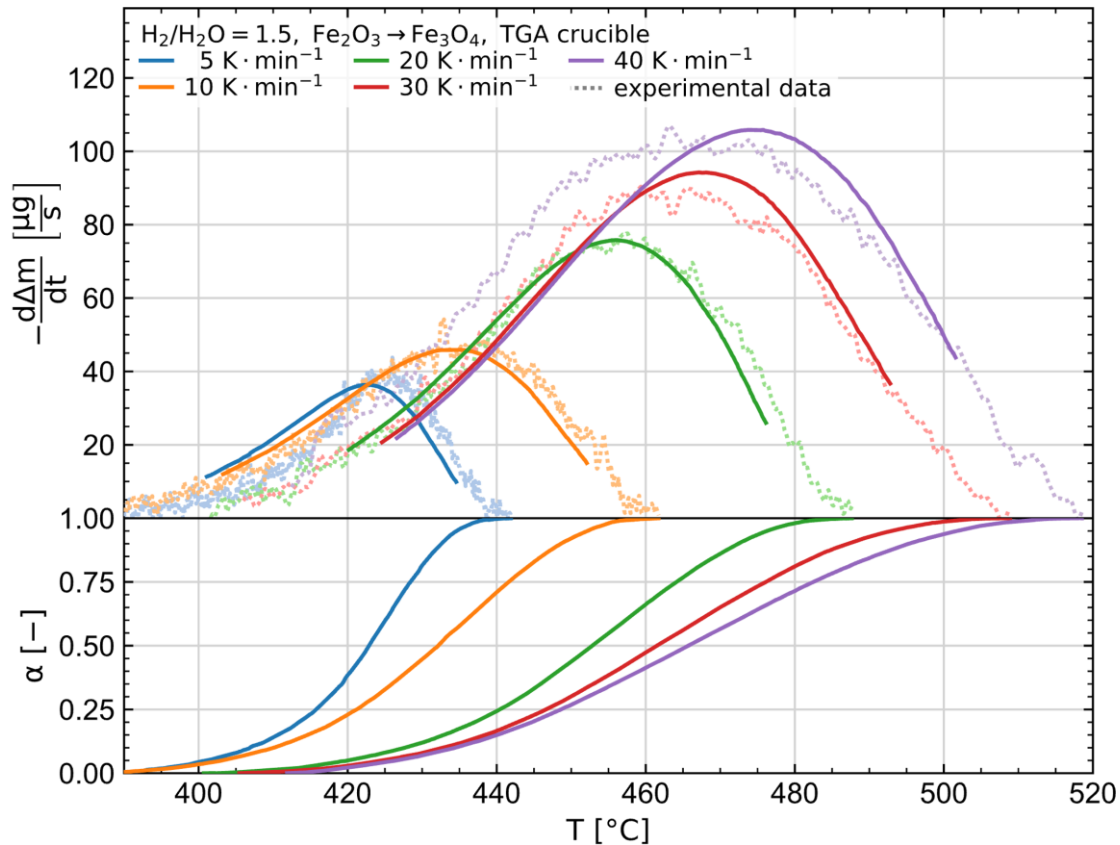
Figure 20: Kinetic evaluation of Fe_2O_3 reduction in a TGA setup at $H_2/H_2O=1.5$

And as before the Arrhenius plot in Figure 21 confirms this by implying a change of the apparent activation energy around 450 °C. The parameters resulting from the model fit stay largely the same. The apparent activation energy computes to 101 kJ·mol^{-1}·K^{-1} and the parameter n in the JMAEK formulation equates to a value of 1.9. The increased reaction kinetics at the higher H_2/H_2O ratios indicate that the reaction rate is influenced by gas diffusion in the sample, considering a constant bulk gas concentration. Even though gas starvation to a certain extent was shown to be present, it influences the reaction in a similar way at different H_2/H_2O ratios.
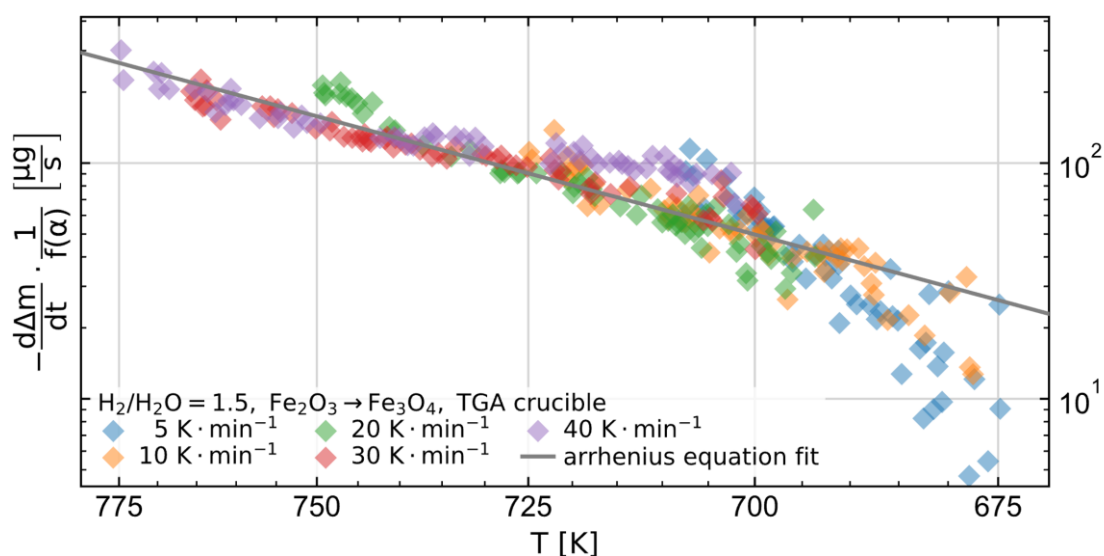
Figure 21: Arrhenius plot for Fe_2O_3 reduction in a TGA setup at H2/H2O=1.5

Figure 22 shows the results for the first reduction step from Fe_2O_3 in an STA crucible. The trials proceeded mainly as expected and in a similar overall manner compared to the trials in the TGA setups. Maximum reaction rates about 1/3 lower for the individual trials mark the most significant difference. Accompanied by a shift of these maxima to higher temperatures, the reaction is significantly slower when performed in STA crucibles. The fit was again achieved with the model after JMAEK. Yet the parameter n equates to 2.4 with this crucible geometry.

The relevant Arrhenius plot for this set of experiments is shown in Figure 23. The individual experiments again do not show a decent correlation with the overall straight representing the Arrhenius equation. The change in the apparent activation energy happens at a similar temperature compared to the experiments performed in TGA setups. The resulting apparent activation energy from the model fit is 46 kJ·mol^{-1}·K^{-1}. As the reaction is generally shifted to higher temperatures for experiments in STA crucibles, this perhaps is consistent with results from experiments in the TGA setup. Yet the present data is not sufficient to allow a definitive statement on whether the apparent activation energies of the different setups represent the same rate limiting mechanism.
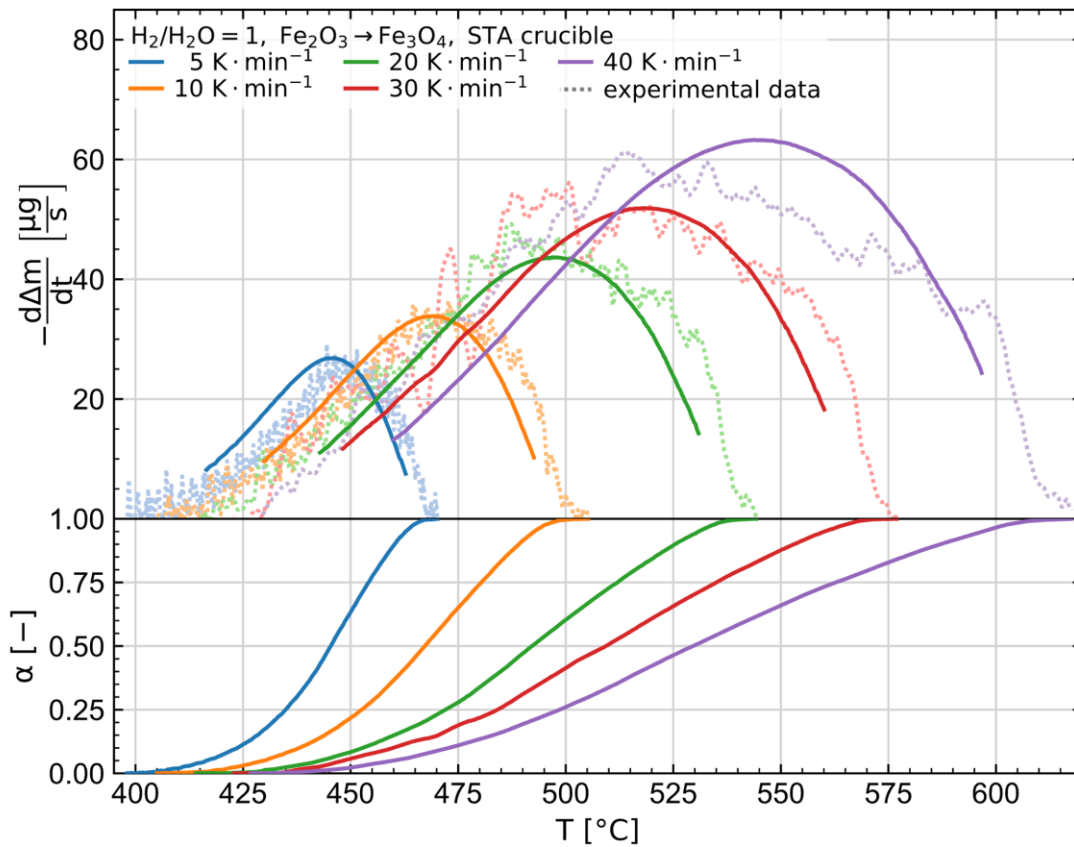
Figure 22: Kinetic evaluation of Fe_2O_3 reduction in an STA crucible at H_2/H_2O=1

In conclusion, however, it should be noted that the setup significantly influences the reaction kinetics in this present case. Therefore, it is questionable, if the setup with an STA crucible generates reliable data for any future use. While a transformation of the results to a different geometry may be possible, the results from the TGA setup seem far superior in this regard.
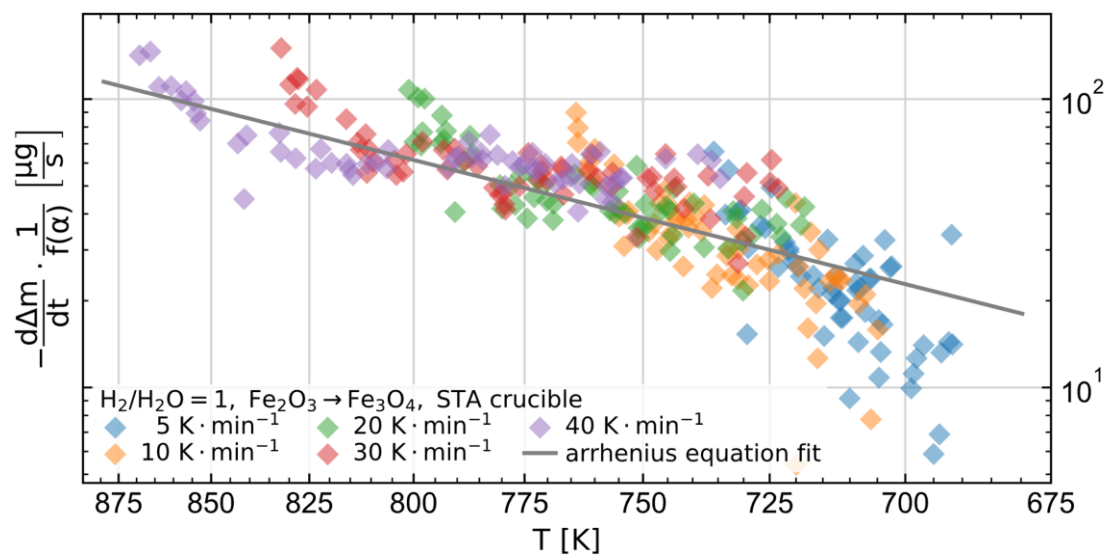
Figure 23: Arrhenius plot for Fe_2O_3 reduction in an STA crucible at H_2/H_2O=1

Kinetic evaluation of the second reduction step to FeO and FeO$_{zf}$

Figure 24 shows the results for the second reduction step of ZnFe$_2$O$_4$. The model fitted onto the data uses the formulation after Šesták-Berggren as is the case for the first reduction step. The resulting parameters from the fitting operation are m=1.9, n=0, and p=-2. This again indicates that the reaction is limited by diffusion in the later stage. The first term in the Šesták-Berggren equation describes that the equation accelerates at the beginning.
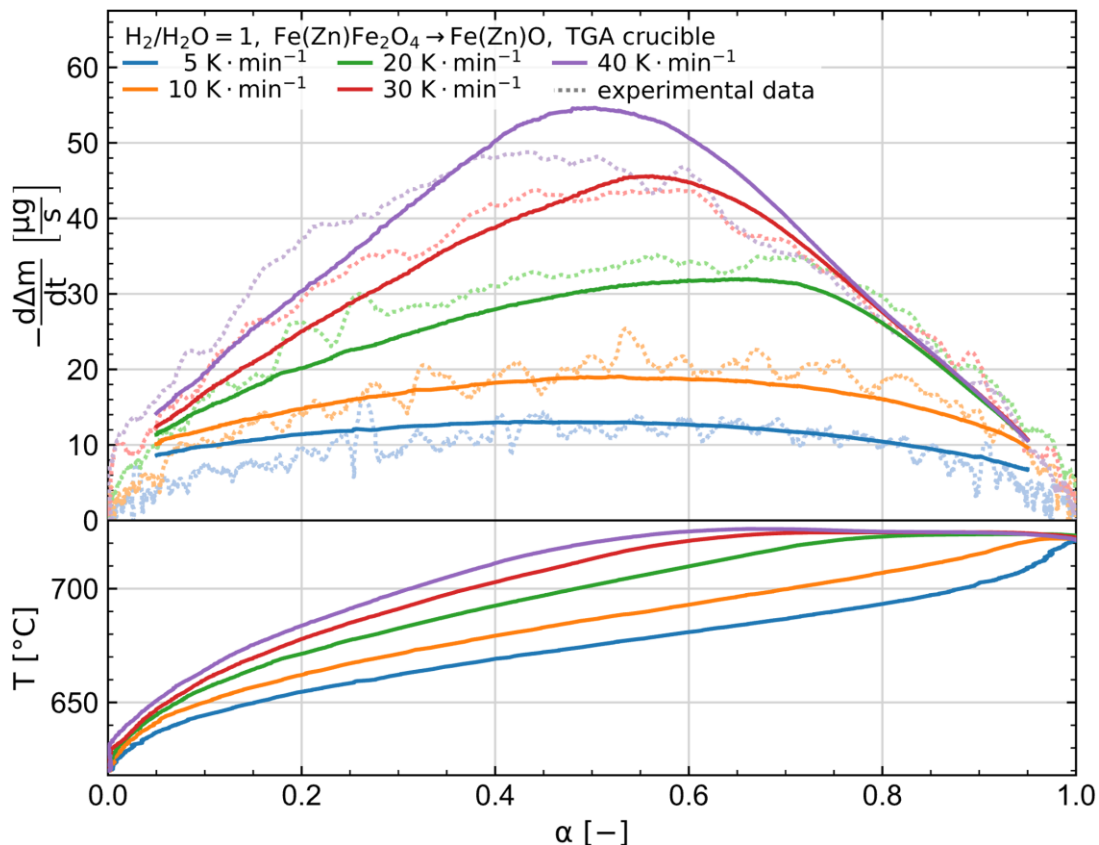
Figure 24: Kinetic evaluation of Fe$_3$O$_{4,zf}$ reduction in a TGA setup at H$_2$/H$_2$O=1

However, compared to the first reaction step the acceleration proceeds slower in this case. The parameter area for this set of experiments is very limited, as the reaction of ZnO proceeds with a notable rate above 720 °C. As the experiments were performed with continuously increasing temperature, the resulting mass loss cannot be easily corrected for the reaction rate of ZnO as it is also temperature dependent. Overall, the reaction proceeds at a faster rate compared to the first reaction step. The model fit is satisfactory although it overestimates the reaction at low temperatures and low fraction conversion. Additionally, at a heating rate of 40 K·min^{-1}, the model underestimates the reaction rate at the start and overestimates the maximum rate. The Arrhenius plot for this set of trials is shown in Figure 25. The single experiments reliably follow the straight depicting the model fitting. The only notable

inconsistency is the slight deviation of the experiment with the lowest heating rate. The result for the apparent activation energy is 248 kJ·mol^{-1}·K^{-1}.
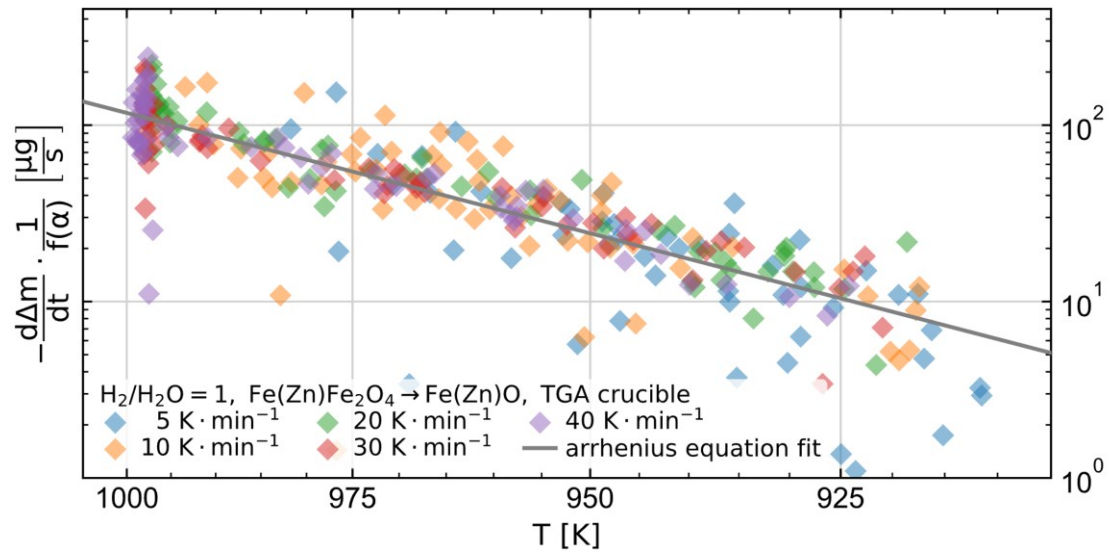
Figure 25: Arrhenius plot for Fe$_3$O$_{4,zf}$ reduction in a TGA setup at H$_2$/H$_2$O=1

The results for the second reduction step of Fe$_2$O$_3$ in the TGA setup at H$_2$/H$_2$O of 1 are shown in Figure 26. The single curves result from the same experiments that were performed for the first set of experiments at these parameters.
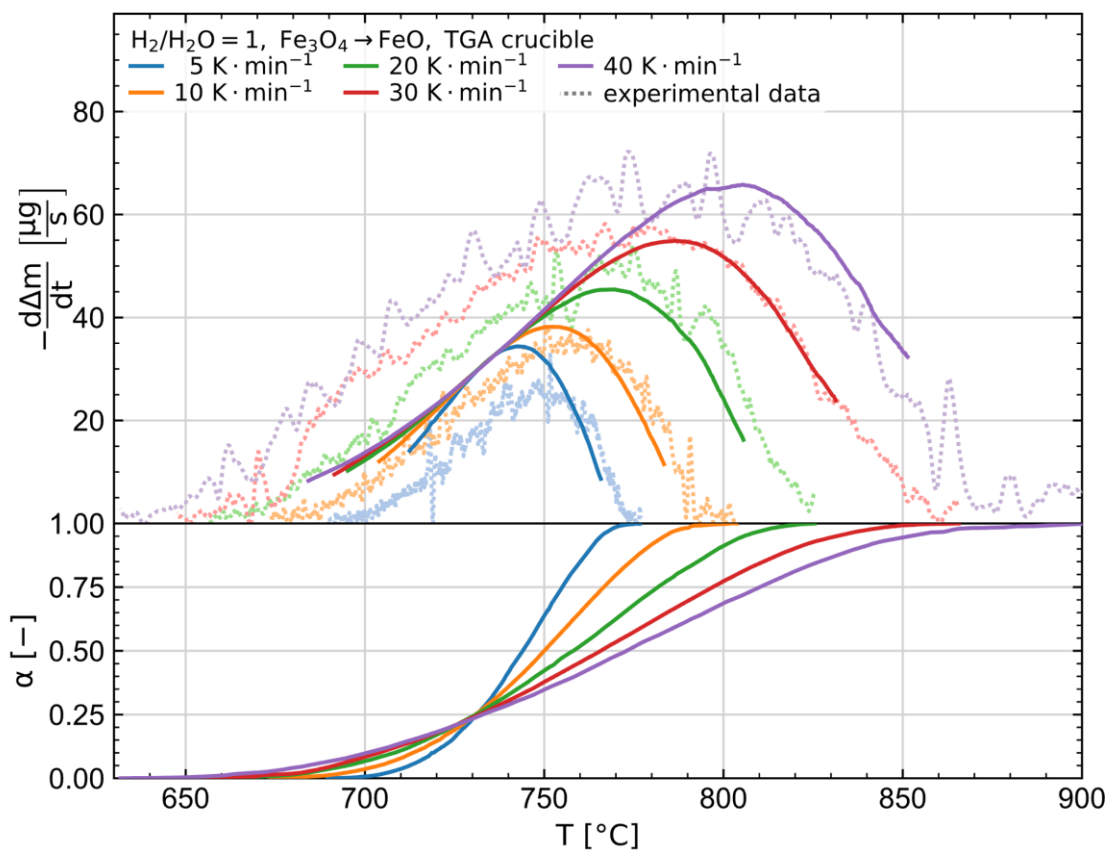
Figure 26: Kinetic evaluation of Fe$_3$O$_4$ reduction in a TAG crucible at H$_2$/H$_2$O=1

The reactions happened in direct succession without leaving the temperature program at a constant heating rate. The single plots present an initially unexpected behaviour. The reaction starts at lower temperatures with increasing heating rates. This signifies that the previous reduction conditions influence the sample properties and can be explained by two possible mechanisms. Either a higher dwell time at lower heating rates promote some form of sintering or the temperature at which the reaction happens influences the morphology of the material. The first option seems unlikely as the overall experiments durations and temperatures are relatively low. Although the high initial surface area and the genesis of the material during the reduction process may result in a denser product phase. The second possibility would indicate that a higher reaction rate during the reduction process leads to an increased surface area of the product. The difference in the reaction rate for the single curves is quite severe and the start of the reaction is shifted by about 50 K. To achieve such a large deviation, the degree of sintering would have to be quite large. It seems therefore more likely that the observed behaviour is caused by the reaction rate during the first reduction step. The corresponding Arrhenius plot is outlined in Figure 27. Although the parameter fit of a kinetic model cannot deliver any reasonable kinetic data, some conclusions can still be drawn from it. The scatter plots for the single experiments are largely inconsistent with the fitted Arrhenius equation. They all seem to follow their own almost linear trend though. The data for this plot is generated by dividing the rate data with the results of evaluating the formulation of the dependency on the fraction conversion. Therefore, the resulting expression for the conversion dependency after JMAEK with n=1.6 seems to be applicable to the data.
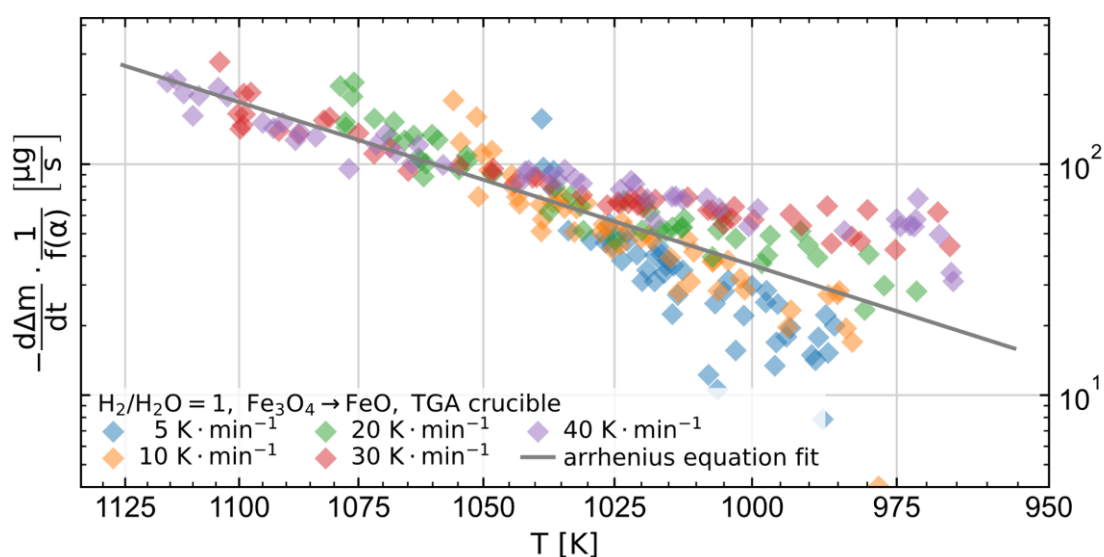
Figure 27: Arrhenius plot for Fe_3O_4 reduction in a TGA setup at $H_2/H_2O=1$

These results are in line with the results from an H_2/H_2O ratio of 1.5 which is shown in Figure 28. The resulting Arrhenius plot for this set of experiments in Figure 29, also corresponds to

these findings. From these results can be concluded that the application of a continuous heating program over the first to reduction steps is an inherent flaw in the experimental design.
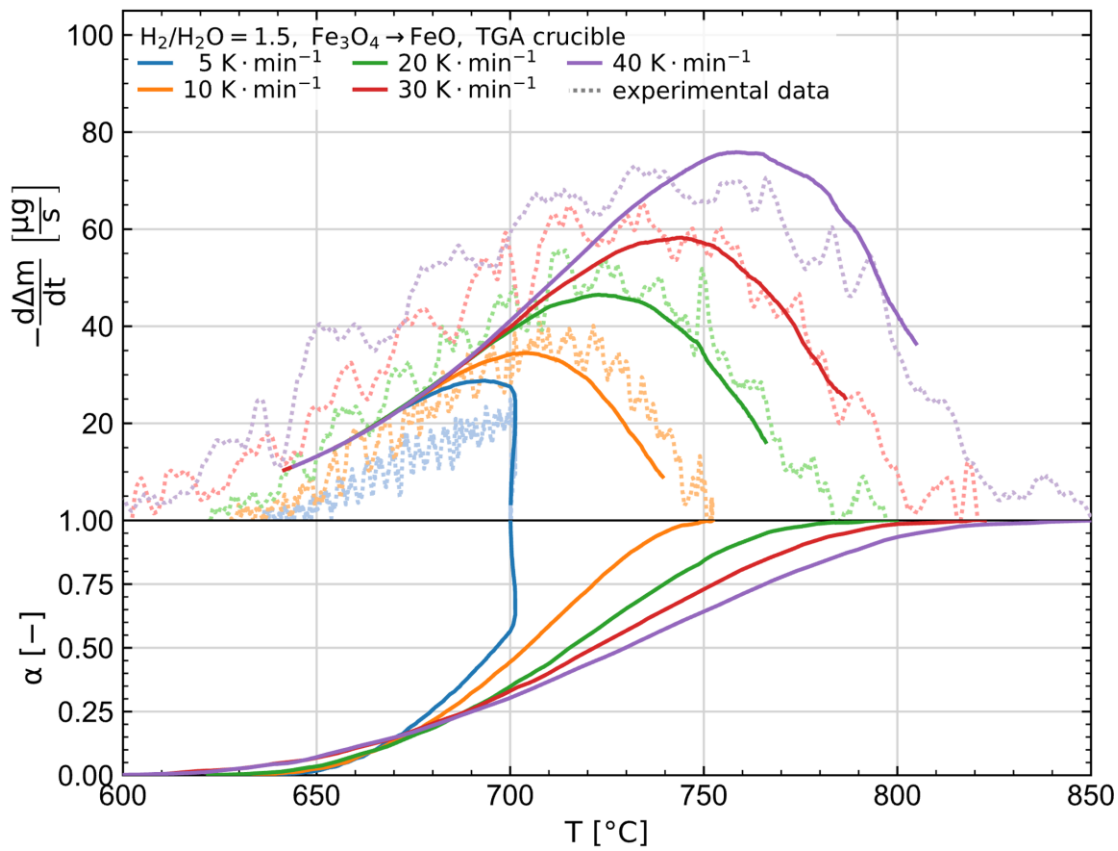
Figure 28: Kinetic evaluation of Fe_3O_4 reduction in a TGA setup at $H_2/H_2O=1.5$

This definitely has to be considered for the fine Fe_2O_3 sample material. However, such a phenomenon was not observed during the reduction trials on $ZnFe_2O_4$.
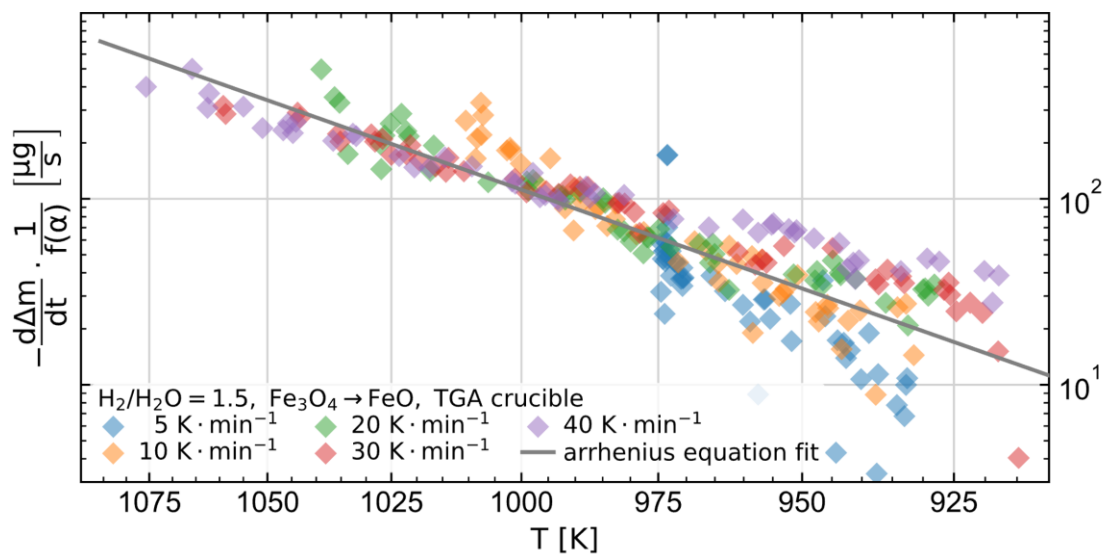
Figure 29: Arrhenius plot for Fe_3O_4 reduction in a TGA setup at $H_2/H_2O=1.5$

The overall rates of the experiments performed at an H_2/H_2O ratio of 1.5 are slightly higher compared to the ones at a ratio of 1. The reaction also shifted to about 50 K lower temperatures, again indicating that the reaction kinetics of the used Fe_2O_3 material during the reduction to FeO are significantly influenced by the gas composition.

The results for the second reaction step performed in STA crucibles are depicted in Figure 30 and the corresponding Arrhenius plot in Figure 31. The reaction proceeds generally at roughly half the reaction rate compared to the TGA setup. This is again accompanied by a shift to overall higher temperatures. The reaction kinetics are therefore significantly worse in an STA crucible compared to the TGA setup. The results also suffer from the problem of the kinetics being dependent on the former reaction conditions. Although the effect is less pronounced in the STA setup. This may be a consequence of the generally lower reaction rates in this case.
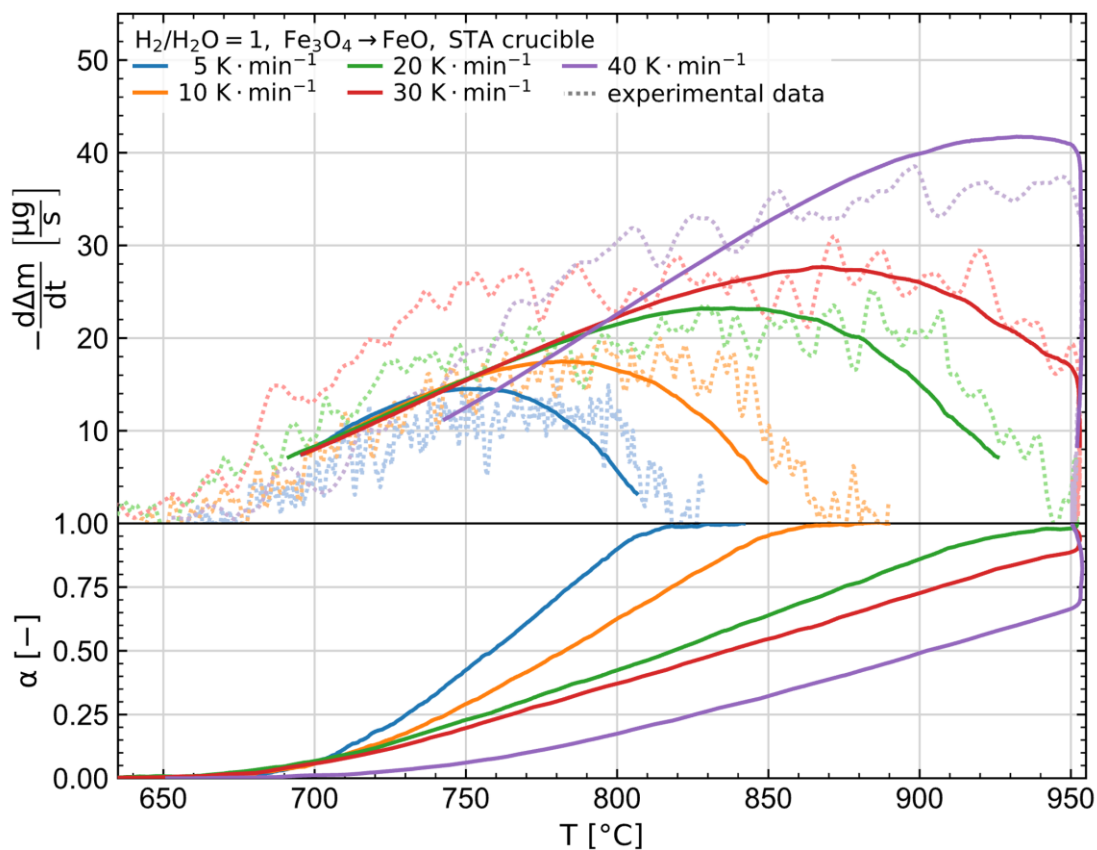
Figure 30: Kinetic evaluation of Fe_3O_4 reduction in an STA crucible at H_2/H_2O=1

The Arrhenius plot for these trials again shows a strong separation of the plots from the single experiments. And the single scatter plots also do not follow a linear trend anymore. This indicates that the model for the dependency on the fraction conversion is not representing the behaviour during the experiments. Consequently, no part of the model can be predicted on basis of the data.
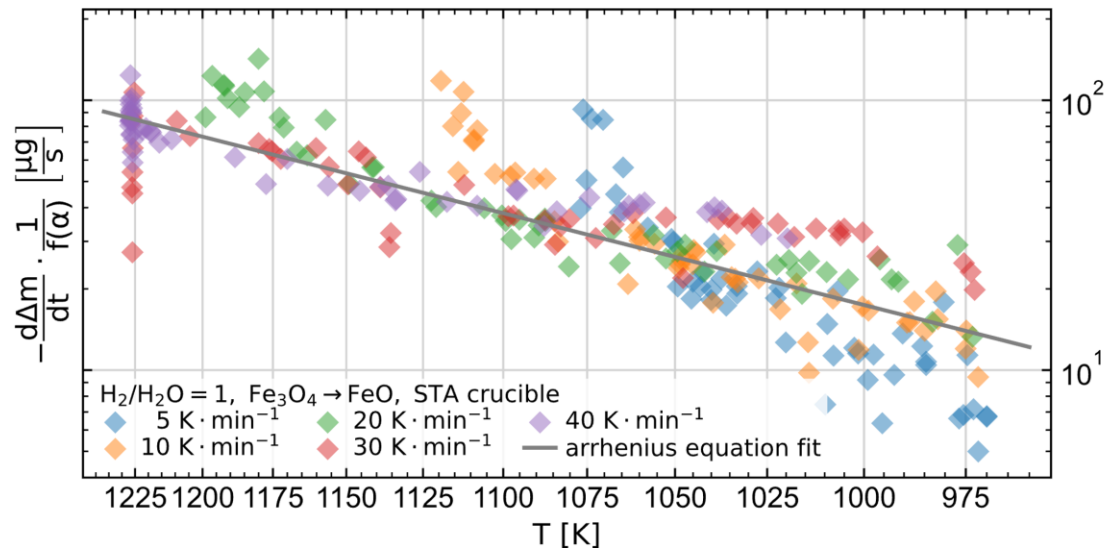
Figure 31: Arrhenius plot for Fe_3O_4 reduction in an STA crucible at $H_2/H_2O=1$

Kinetic evaluation of the final reduction step to metallic Fe

The results for the last reduction step of the experiments with $ZnFe_2O_4$ are illustrated in Figure 32. The reactions started with the switch to an H_2/H_2O ratio of 9 with FeO_{zf} as the initial compound. The gas ratio was changed after adjusting the temperatures to the values for the isothermal segments. The maximum temperature at which the experiments can be performed is limited by the simultaneous reduction of ZnO. Above 740 °C the transition from the reduction of FeO_{zf} to ZnO becomes so blurred that they cannot be reliably separated.
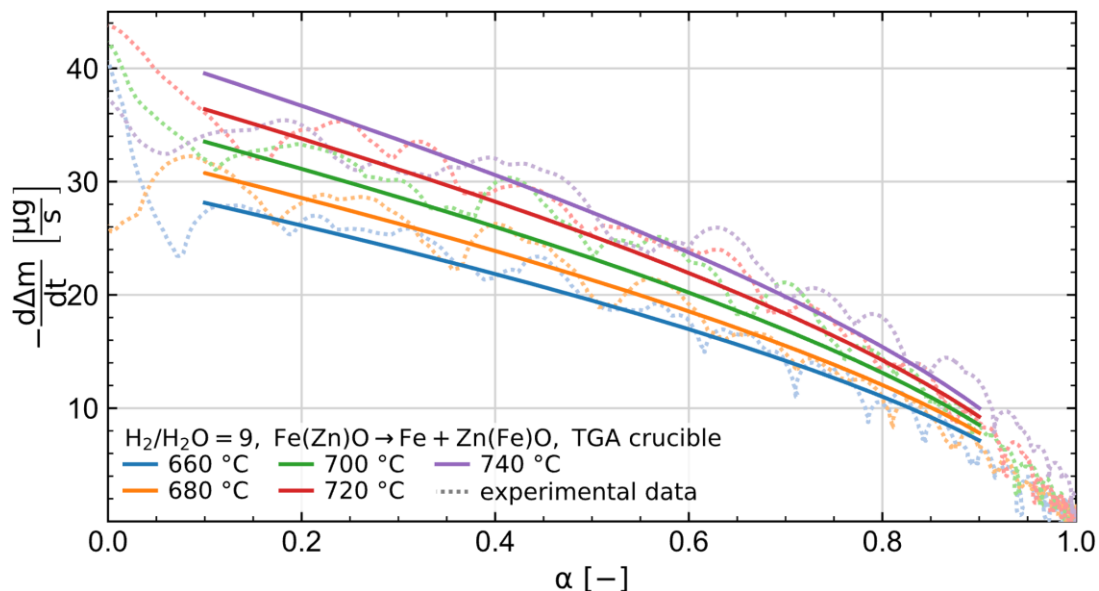
Figure 32: Kinetic evaluation of FeO_{zf} reduction in a TGA setup at $H_2/H_2O=9$

A geometric contraction model was fitted obtaining a value of 2.65 for the parameter n. The curves calculated from the model represent the trend of the experiments to a satisfactory level.

Because of the small parameter area though, the validity of the resulting model is questionable. Figure 33 shows the corresponding Arrhenius plot for these experiments. While the experiments follow the fitted straight to a certain extent, their correlation is also not conclusive of a reliable kinetic model. The apparent activation energy resulting from the fit is 33 $kJ \cdot mol^{-1} \cdot K^{-1}$.
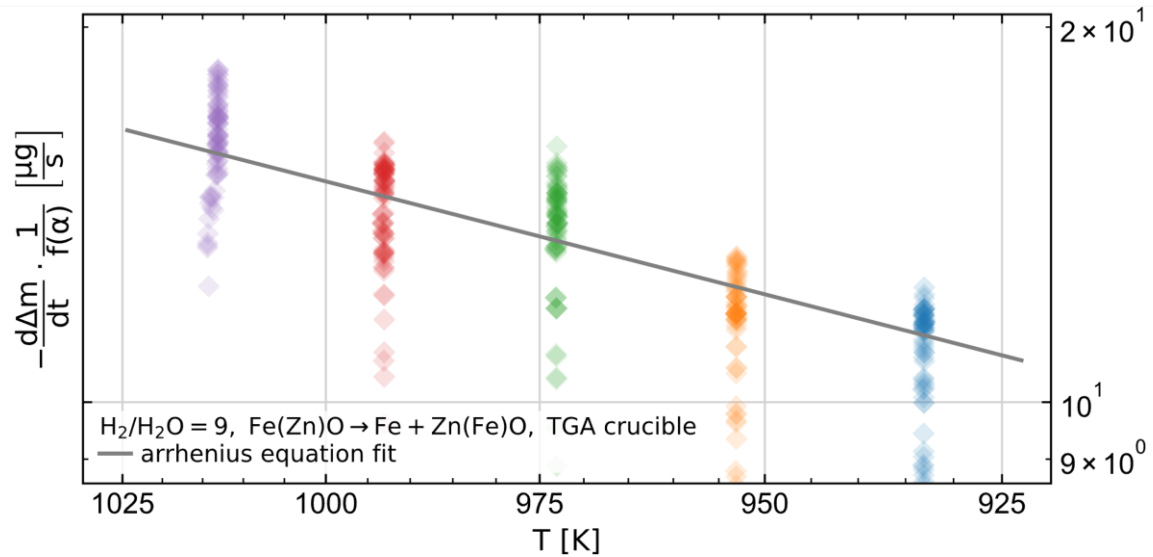
Figure 33: Arrhenius plot for FeO_{zf} reduction in a TGA setup at $H_2/H_2O=9$

The reduction from FeO to Fe was also evaluated. The starting material was the product of the experiments reducing Fe_2O_3 at an H_2/H_2O ratio of 1.5. Figure 34 shows the resulting plot where the equation for geometric contraction is used to model the dependency on the fraction conversion. The parameter n equals a value of 1.8 and the apparent activation energy to 35 $kJ \cdot mol^{-1} \cdot K^{-1}$.
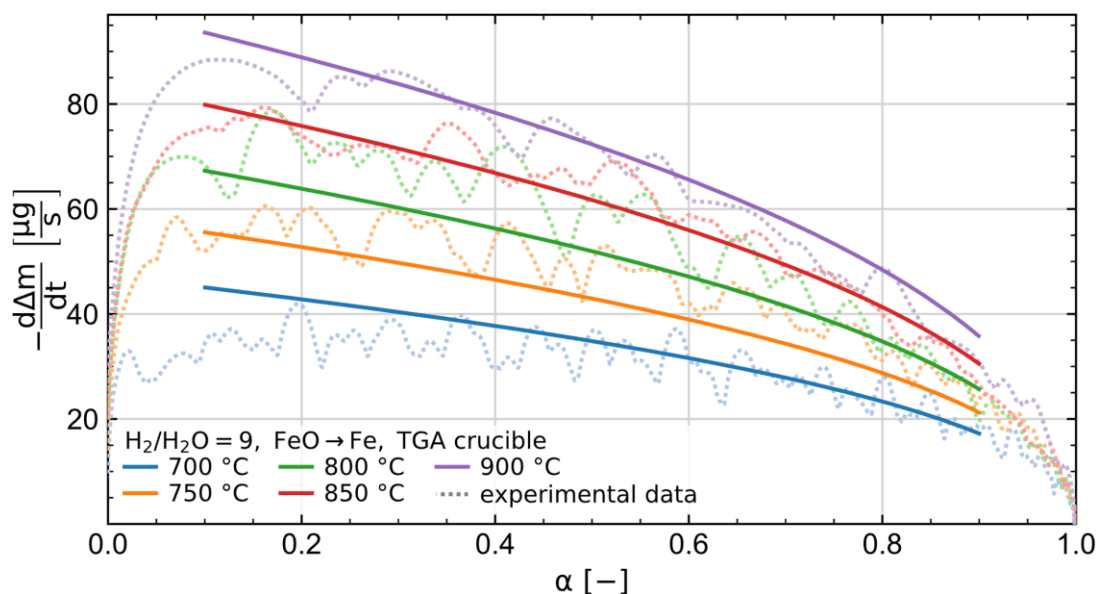
Figure 34: Kinetic evaluation of FeO reduction in a TGA setup at $H_2/H_2O=9$

The model overestimates the reaction rate of the experiment at 700 °C at the beginning of the reaction and slightly underestimates the rate at 750 °C and 800 °C throughout the experiments. Figure 35 shows the Arrhenius plot for this experiment. It exhibits the same discrepancies discussed for the model fit of the single reactions. There seems to be a change in mechanism in the investigated temperature interval. Although, any further statement would need additional data.

The results of the parameter fit indicate that the FeO sample follows the formulation for a contraction area. But there also appears to be at least one overlapping mechanism that skews the results. The calculated value for FeO_{zf} sits in between the values for 2- and 3-dimensional contraction and therefore may be interpreted as a mixture of both, while the influence of additional mechanisms is also likely.
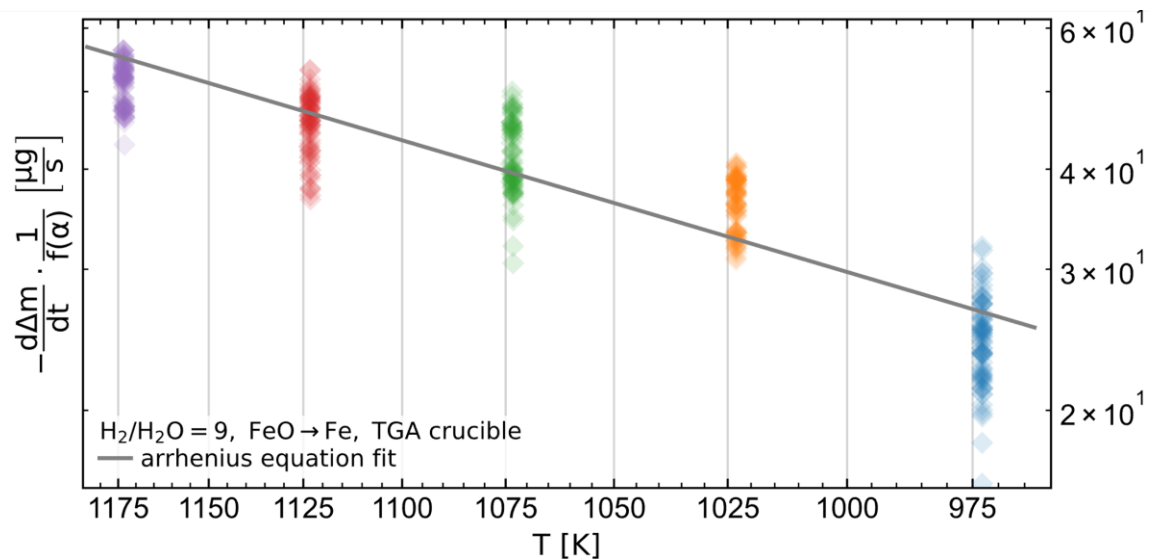
Figure 35: Arrhenius plot for FeO reduction in a TGA setup at H_2/H_2O=9

4.3 Reduction behaviour of EAF dust

To compare the kinetic behaviour of ZnF_2O_4 and EAF dust, two experiments with samples of the latter were performed. The mass loss, mass loss rate, and temperature program for these experiments are shown in Figure 36. The first step was heated up to 620 °C with a heating rate of 20 K·min^{-1} and an H_2/H_2O ratio of 1. After reaching equilibrium conditions the samples were further heated up to 720 °C and 780 °C respectively. After holding for some time to illustrate the constant mass loss due to ZnO reduction, the gas composition was changed to an H_2/H_2O ratio of 9. While the EAF dust sample nr. 1 was reduced until equilibrium conditions were reached, sample nr. 2 was stopped at 80 % conversion.

Two distinct rate peaks are visible for the first reduction step, the first of which has its maximum at the transition from the heating ramp to the isothermal segment. The chemical analysis of the calcined sample material in Table 3 shows no elements whose compounds would lead to

such behaviour. There is an increase in mass though before the start of the experiment after switching on the H_2O gas flow. This increase corresponds to the mass loss caused by the first short peak. This indicates the formation of a hydroxide phase during the initial heating which is decomposed again at elevated temperatures. While 2 peaks could theoretically mean the presence of both Fe_2O_3 and $ZnFe_2O_4$, the mass loss of all three consecutive steps would need to correlate with the mass loss steps of Fe_2O_3. The mass loss during the first step however is too less to support this assumption. The reduction process signified by the second peak proceeds rather slow when compared to the kinetics of the pure samples. The maximum rates reach only about a tenth of the rate which was achieved during the reduction of $ZnFe_2O_4$ at a similar temperature.
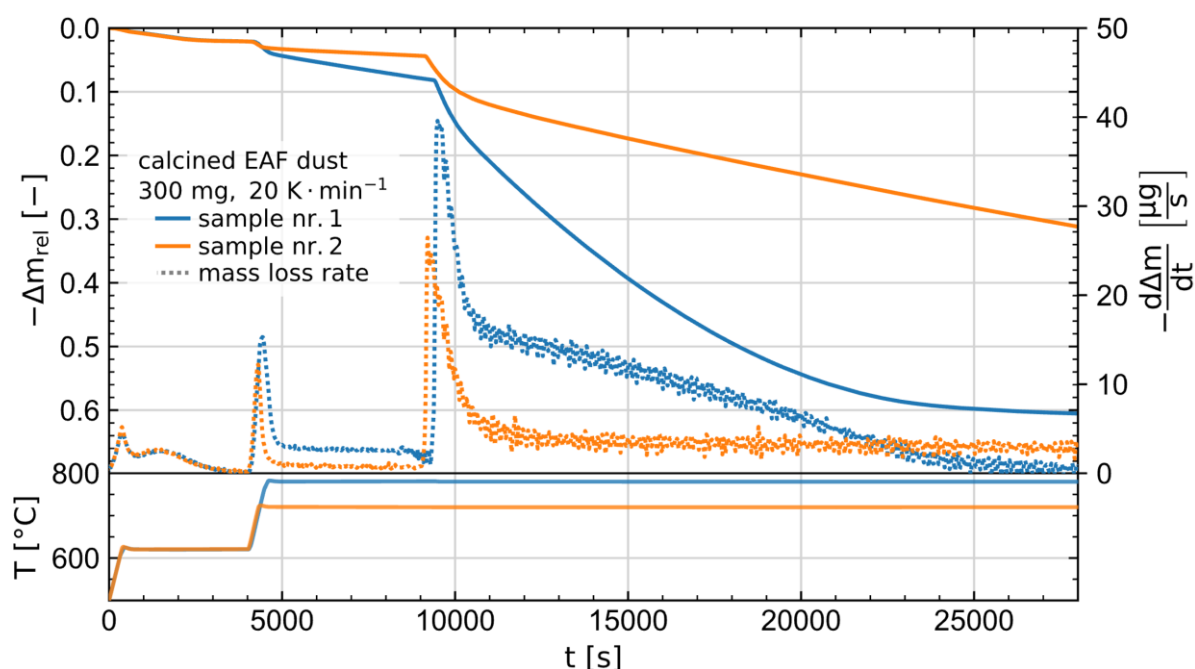
Figure 36: Mass loss curves of the reduction trials on EAF dust

For the second reduction step, only a single peak is visible for every experiment. Its rate peaks at approximately one-fifth of the peak observed during the reduction of Fe_2ZnO_4 at a similar temperature. At 780 °C the reaction of ZnO proceeds already with a significant rate at the H_2/H_2O ratio of 1 while it is negligible at 720 °C.

There are a few factors that may cause the overall slower reduction kinetics for EAF dust during the first two reduction steps. The calcined EAF dust sample has a significantly lower specific surface area compared to the pure sample materials. This is especially relevant considering that the kinetic evaluation for $ZnFe_2O_4$ indicated the rate to be controlled by diffusion. The EAF dust sample contains a large amount of ZnO which does not take part in this early stage of reduction. While Fe_2O_3 and $ZnFe_2O_4$ leave room for the diffusion of gaseous reactants after their reduction, ZnO obstructs the diffusive gas flow into the sample. The same is true for other inert oxides present in the sample. Additionally, these oxides may influence the kinetic

behaviour when forming solid solutions or compounds with Fe_2O_3 or $ZnFe_2O_4$. Finally, there is less total Fe present compared to $ZnFe_2O_4$ which may lead to a slower reaction rate.

The reduction to metallic Fe proceeds rather fast after switching to a gas ratio of 9. At 780 °C the reduction of ZnO proceeds at a considerable rate parallel to the reaction of FeO_{zf}. Subtracting the constant rate of ZnO reaction from the single peaks, the overall rate for the reduction of FeO_{zf} for EAF dust is about the same as for $ZnFe_2O_4$. Although considering the 60 K lower temperature, the kinetics of EAF dust are also overall worse for the last reduction step.

5 Summary and Outlook

The objective of this work was to gather kinetic information on the reduction of EAF dust with H_2. It was possible to study the reaction kinetics of powdered $ZnFe_2O_4$ and EAF dust during the selective stepwise reduction in an H_2-H_2O-N_2 atmosphere on basis of thermogravimetric experiments. Additionally, the reduction kinetics of Fe_2O_3 powder were investigated under similar conditions to further elaborate the findings.

Using a relatively small crucible filled with loose material proved to be an unreliable setup. This is for example the case with typical STA specimen holders. It is favourable to investigate powdered materials in compacted form to guarantee an adequate gas flow around the sample. The reduction behaviour of $ZnFe_2O_4$ differs vastly from that of Fe_2O_3. Fe^{2+} and Zn^{2+}-ions are to a large extent interchangeable in the spinel phase. Additionally, FeO and ZnO show significant solubility in each other. The decomposition of $ZnFe_2O_4$ is therefore a rather complex process as the equilibrium composition of the products in the reaction sequence varies with temperature. This leads to generally less favourable kinetic conditions for the Fe-oxide in $ZnFe_2O_4$ compared to Fe_2O_3.

The kinetics for the reduction of $ZnFe_2O_4$ to $Fe_3O_{4,zf}$ are shown to be governed by diffusion as the rate-limiting step in the temperature range of 460–620 °C. The reduction of $Fe_3O_{4,zf}$ to FeO_{zf} in the temperature interval of 620–720 °C is also suggested to be controlled by diffusion. This only describes the later stage of the reduction processes while the rate at the start of the reaction is limited by an acceleratory phenomenon. These findings are based on the curve fitting results of the kinetic models and substantiated by the high apparent activation energy of 316 $kJ·mol^{-1}·K^{-1}$ and 248 $kJ·mol^{-1}·K^{-1}$ for the first and the second step respectively.

The reduction of FeO_{zf} to Fe proceeds according to a geometric contraction model between 660 and 740 °C. The evaluation results in an apparent activation energy of 33 $kJ·mol^{-1}·K^{-1}$. The reduction of FeO proceeds similarly to that of FeO_{zf}. Their overall reduction rates are comparable and while the kinetic model slightly differs, the apparent activation energy was found to be 35 $kJ·mol^{-1}·K^{-1}$.

EAF dust behaves similar to $ZnFe_2O_4$ during the reduction with H_2. While impurities influence the reaction rates of the individual steps and cause an overall slower reduction, the selective reduction of Fe-oxides seems feasible at reasonable times.

Gas composition and flow rates were not ideal during this study due to several limitations in the experimental setup. Especially, the behaviour of EAF dust, $ZnFe_2O_4$, as well as the kinetic evaluation would benefit from further experiments with higher H_2 contents and higher gas flow rates. Additional experiments at various H_2/H_2O ratios should also be carried out to gain further understanding of the reduction mechanisms.

The temperature range in which the reactions were studied could be more extensive. The study of the reaction kinetics, especially the model fit, should better be studied under isothermal conditions. Thus, larger parameter areas for temperature, and H_2/H_2O ratio could be investigated. Isothermal temperature programs would also increase the comparability of single experiments, as reactions tend to diverge in fraction conversion at a given temperature during continuous heating programs. However, the application of isothermal temperature programs together with H_2O in the gas stream requires a three-way valve in the input gas duct. Otherwise, a controlled gas composition cannot be guaranteed due to the reaction time at the start of the H_2O gas flow.

The results of the kinetic model fit on the $ZnFe_2O_4$ reduction reactions are overall satisfactory, but they would benefit from further studies with an adjusted experimental setup. Additional kinetic investigations for the reduction of EAF dust, especially an extensive study of the involved reaction mechanisms, are necessary to establish a potential industrial process.

6 Bibliography

[1] Sofilić T. et al.: Characterization of steel mill electric-arc furnace dust. Journal of hazardous materials, 109 (2004), 59–70.

[2] Brandner U., J. Antrekowitsch and M. Leuchtenmueller: A review on the fundamentals of hydrogen-based reduction and recycling concepts for electric arc furnace dust extended by a novel conceptualization. International Journal of Hydrogen Energy, 46 (2021), 31894–31902.

[3] Gao J.-T. et al.: Experimental study on solid state recovery of metallic resources from EAF dust. Ironmaking & Steelmaking, 39 (2012), 446–453.

[4] Pickles C. A.: Thermodynamic analysis of the separation of zinc and lead from electric arc furnace dust by selective reduction with metallic iron. Separation and Purification Technology, 59 (2008), 115–128.

[5] ITOH S. and T. AZAKAMI: Application of Iron-Reduction Distillation Reaction to Zinc Oxide. Journal of the Mining Institute of Japan, 104 (1988), 297–302.

[6] Xia D. K. and C. A. Pickles: Caustic Roasting and Leaching of Electric Arc Furnace Dust. Canadian Metallurgical Quarterly, 38 (1999), 175–186.

[7] Sasamoto H. et al.: New technology for treating EAF dust by a vacuum heating reduction process. Revue de Métallurgie, 95 (1998), 1225–1230.

[8] Chung-Lee L. and T. Min-Shing: A crystal phase study of zinc hydroxide chloride in electric-arc-furnace dust. Journal of Materials Science, 28 (1993), 4562–4570.

[9] Machado J. G. M. S. et al.: Chemical, physical, structural and morphological characterization of the electric arc furnace dust. Journal of hazardous materials, 136 (2006), 953–960.

[10] Suetens T. et al.: Formation of the $ZnFe_2O_4$ phase in an electric arc furnace off-gas treatment system. Journal of hazardous materials, 287 (2015), 180–187.

[11] Kashiwaya Y. et al.: Thermodynamic Analysis on the Dust Generation from EAF for the Recycling of Dust. ISIJ International, 44 (2004), 1774–1779.

[12] Tsubouchi N. et al.: Chemical characterization of dust particles recovered from bag filters of electric arc furnaces for steelmaking: some factors influencing the formation of hexachlorobenzene. Journal of hazardous materials, 183 (2010), 116–124.

[13] Yoo J.-M. et al.: Kinetics of the Volatilization Removal of Lead in Electric Arc Furnace Dust. MATERIALS TRANSACTIONS, 46 (2005), 323–328.

[14] Lin X. et al.: Pyrometallurgical recycling of electric arc furnace dust. Journal of Cleaner Production, 149 (2017), 1079–1100.

[15] Buzin P. J. W. K. de, N. C. Heck and A. C. F. Vilela: EAF dust: An overview on the influences of physical, chemical and mineral features in its recycling and waste incorporation routes. Journal of Materials Research and Technology, 6 (2017), 194–202.

[16] Bale C. W. et al.: FactSage thermochemical software and databases, 2010–2016. Calphad, 54 (2016), 35–53.

[17] Polsilapa S., D. R. Sadedin and P. Wangyao: Thermodynamics Analysis for the Zinc Ferrite Reduction by Hydrogen. High Temperature Materials and Processes, 30 (2011), 587–592.

[18] Hill C. G. and T. W. Root: Introduction to Chemical Engineering Kinetics & Reactor Design. Wiley, Hoboken, New Jersey (2014).

[19] Scott H. F.: Elements of Chemical Reaction Engineering. In: Prentice Hall international series in the physical and chemical engineering sciences. Prentice Hall (2016).

[20] Vyazovkin S. et al.: ICTAC Kinetics Committee recommendations for performing kinetic computations on thermal analysis data. Thermochimica Acta, 520 (2011), 1–19.

[21] Khawam A. and D. R. Flanagan: Solid-state kinetic models: basics and mathematical fundamentals. The journal of physical chemistry. B, 110 (2006), 17315–17328.

[22] Šesták J. and G. Berggren: Study of the kinetics of the mechanism of solid-state reactions at increasing temperatures. Thermochimica Acta, 3 (1971), 1–12.

[23] Bogdandy L. and H.-J. Engell: The Reduction of Iron Ores. Springer Berlin Heidelberg, Berlin, Heidelberg (1971).

[24] Tong F. L. and P. Hayes: Mechanisms of the Reduction of Zinc Ferrites in H_2/N_2 Gas Mixtures. Mineral Processing and Extractive Metallurgy Review, 28 (2006), 127–157.

[25] Kazemi M. and Du Sichen: Investigation of Selective Reduction of Iron Oxide in Zinc Ferrite by Carbon and Hydrogen. Journal of Sustainable Metallurgy, 2 (2016), 73–78.

[26] Pineau A., N. Kanari and I. Gaballah: Kinetics of reduction of iron oxides by H2. Thermochimica Acta, 447 (2006), 89–100.

[27] Pineau A., N. Kanari and I. Gaballah: Kinetics of reduction of iron oxides by H2. Thermochimica Acta, 456 (2007), 75–88.

[28]   Wexler A.: Vapor Pressure Formulation for Water in Range 0 to 100 °C. A Revision.
       Journal of research of the National Bureau of Standards. Section A, Physics and
       chemistry, 80A (1976), 775–785.

[29]   Newbury D. E. and N. W. M. Ritchie: Is scanning electron microscopy/energy
       dispersive X-ray spectrometry (SEM/EDS) quantitative? Scanning, 35 (2013), 141–168.

[30]   Virtanen P. et al.: SciPy 1.0: fundamental algorithms for scientific computing in Python.
       Nature methods, 17 (2020), 261–272.

7 Table of Figures

8 Table Directory